

A comprehensive single-cell map of T cell exhaustion-associated immune environments in human breast cancer

Sandra Tietscher

University of Zurich

Johanna Wagner

DKFZ and NCT <https://orcid.org/0000-0002-5087-3657>

Tobias Anzeneder

PATH Biobank

Claus Langwieder

Pathologie Josefshaus

Martin Rees

Pathologie Josefshaus

Bettina Sobottka

University Hospital Zurich

Natalie de Souza

University of Zurich

Bernd Bodenmiller (✉ bernd.bodenmiller@imls.uzh.ch)

University of Zürich, <https://orcid.org/0000-0002-6325-7861>

Article

Keywords: Breast cancer, T cell exhaustion, tumor immune microenvironment, Luminal B, single-cell analysis, multiplexed imaging

Posted Date: January 5th, 2022

DOI: <https://doi.org/10.21203/rs.3.rs-1155834/v1>

License: © ⓘ This work is licensed under a Creative Commons Attribution 4.0 International License.

[Read Full License](#)

A comprehensive single-cell map of T cell exhaustion-associated immune environments in human breast cancer

2

4 Sandra Tietscher^{1,2,3}, Johanna Wagner^{1,4}, Tobias Anzeneder⁵, Claus Langwieder⁶, Martin Rees⁶, Bettina Sobottka⁷, Natalie de Souza^{1,2} and Bernd Bodenmiller^{1,2*}

6

8

1. Department of Quantitative Biomedicine, University of Zurich, Zurich, Switzerland

10

2. Institute for Molecular Health Sciences, ETH Zurich, Zurich, Switzerland

12

3. Life Science Zurich Graduate School, ETH Zurich and University of Zurich, Zurich, Switzerland

14

4. Department of Translational Medical Oncology, German Cancer Research Center (DKFZ) and National Center for Tumor Diseases (NCT) Heidelberg, Heidelberg, Germany

16

5. Patients' Tumor Bank of Hope (PATH), Munich, Germany

6. Pathology at Josefshaus, Dortmund, Germany

18

7. Department of Pathology and Molecular Pathology, University Hospital Zurich, Zurich and University of Zurich, Switzerland

20

*correspondence to bernd.bodenmiller@uzh.ch

22 **ABSTRACT**

24 Immune checkpoint therapy in breast cancer remains restricted to triple negative patients, and
26 long-term clinical benefit is rare. The primary aim of immune checkpoint blockade is to prevent
28 or reverse exhausted T cell states, but the causes and implications of T cell exhaustion in
30 breast tumors are not well understood. Here, we used single-cell transcriptomics combined
32 with imaging mass cytometry to comprehensively study exhausted and non-exhausted
34 immune environments in human breast tumors, with a focus on Luminal subtypes. We found
36 that the presence of a PD-1^{high} exhaustion-like T cell phenotype was indicative of an
38 inflammatory immune environment with a characteristic cytotoxic profile and spatial features.
40 Accumulation of natural killer T cells and increased myeloid cell activation in exhausted
immune environments provide further support for tissue inflammation in these environments.
Consistent with this, our comprehensive map of cellular interactions within the breast tumor
microenvironment revealed elevated immunomodulatory, chemotactic, and cytokine signaling
in exhausted environments. These data reveal fundamental differences between exhausted
and non-exhausted immune environments within Luminal breast cancer, and show that
expression of PD-1 and CXCL13 on T cells, and MHC-I – but not PD-L1 – on tumor cells are
strong distinguishing features between these environments; these factors are potential new
biomarkers for patient stratification.

42

KEYWORDS

44

46 Breast cancer, T cell exhaustion, tumor immune microenvironment, Luminal B, single-cell
analysis, multiplexed imaging

48 INTRODUCTION

50 Immune checkpoint blockade therapies have improved patient outcomes in many human
52 cancer types¹⁻⁴. Breast cancer is an exception, previously believed to be due to poor
54 immunogenicity⁵, but several studies have identified a strong influence of the immune infiltrate
56 on breast cancer progression^{6,7}. T cell infiltration in particular impacts patient survival for all
58 breast cancer subtypes, but the effect on prognosis may be positive or negative depending on
60 the subtype⁸, highlighting the complexity of the tumor-immune interaction. Recently,
62 atezolizumab and pembrolizumab, two checkpoint inhibitors targeting the PD-1/PD-L1
pathway, have been approved for patients with triple-negative breast cancer⁹. These
treatments increase progression-free survival by several months, but most patients do not gain
long-term clinical benefit, and no approved immunotherapeutic options currently exist for
patients with other breast cancer subtypes. Our understanding of the mechanisms of
resistance or response to immunotherapy is incomplete, as is our knowledge of the complex
cellular interactions in the tumor immune microenvironment (TIME). In order to design new
immunotherapies and to effectively use existing ones for luminal breast cancer patients, it is
critical to understand the TIME as a whole.

64 T cells make up a large part of the immune infiltrate in most solid tumors, including breast
66 tumors⁸, and provide an important line of defense against cancer cells. Upon activation,
68 cytotoxic T lymphocytes (CTLs) can exert their effector function through cytolytic molecules
70 such as granzymes and granulysin or via inflammatory cytokines such as IFN- γ and TNF-
72 α ^{10,11}. At sites of chronic inflammation – such as tumors – where the elimination of target cells
74 fails and T cell receptor (TCR) signaling persists, T cells may become “exhausted”, a cellular
76 state characterized by an elevated co-expression of inhibitory checkpoint receptors such as
78 PD-1, CTLA-4, Tim-3, and LAG-3¹². Prevention or reversal of T cell exhaustion – also termed
T cell dysfunction – is the primary aim of most immune checkpoint blockade therapies¹².
Originally discovered under conditions of viral infection, T cell exhaustion is associated with
reduced effector functions. Although loss of proliferative potential was thought to be a
characteristic of exhausted T cells, recent evidence suggests that they may still proliferate in
human tumors^{13,14} and that T cells with an exhausted phenotype expand after anti-PD1
treatment in breast tumors¹⁵, but the extent to which these cells retain their anti-tumor functions
is unclear¹⁶.

80 Myeloid cells are also present in the immune infiltrate in most breast tumors, with pro- and
82 anti-tumor effects reported¹⁷. Tumor-associated macrophages (TAMs) can directly suppress
84 T cell responses by expression of PD-L1 and other immunomodulatory molecules, or indirectly
via recruitment of regulatory T cells (T_{regs}). Dendritic cells (DCs) prime anti-tumor T cell
function by surface-presentation of tumor-derived antigens¹⁸. Myeloid cells may also promote
angiogenesis and tissue remodeling¹⁹, and other immune cell types like B cells and natural
killer (NK) cells further add to the complexity of immune-mediated effects on tumors.

86 Recent technological developments allow for increasingly robust and comprehensive single-
88 cell analysis of tumor microenvironments at the transcriptional and protein levels²⁰⁻²²,
90 facilitating the investigation of cell type abundances, cellular phenotypes, and cell-to-cell
communication. Spatially resolved multiplexed methods further enable the study of cellular
neighborhoods and spatially defined tissue patterns such as tertiary lymphoid structures (TLS)
in cancer²³⁻²⁶. Although transcriptomic studies have provided insight into the immune

92 composition of both treatment naïve and anti-PD1 treated breast tumors at the single-cell
level^{15,27,28}, a systematic analysis of exhausted and non-exhausted TIMEs and a clinically
94 established TIME-based classification system for patient stratification are missing. In previous
work, we used mass cytometry-based cellular phenotyping to classify (mainly luminal) breast
96 tumors into three groups based on infiltrating T cell and myeloid cell phenotypes²⁹. One group
showed strong enrichment of an exhaustion-like T cell phenotype. This group accounted for
98 around 13% of all tumors and included both ER⁺ and ER⁻ tumors and might be amenable to
immune checkpoint inhibitor therapy. A second group, accounting for 48% of all tumors, also
100 contained a high number of T cells but did not display signs of immune exhaustion.

To deeply characterize the TIME in (luminal) breast cancer and to study which cell-to-cell
102 interactions contribute to an exhausted TIME state, we used single-cell RNA sequencing
(scRNA-seq) combined with imaging mass cytometry (IMC) to systematically analyse the
104 TIME of breast tumors with and without signs of T cell exhaustion (called “exhausted” and
“non-exhausted” environments hereafter). We discovered that T cells expressing exhaustion
106 markers display hallmarks of tumor reactivity and proliferation, and that their presence
coincides with elevated MHC-I expression on tumor cells. High levels of expression of *GZMB*
108 and *FASL* (encoding Granzyme B and Fas ligand) but low levels of *IFNG* and *TNF* (encoding
Interferon- γ and TNF- α) in these exhausted-like T cells are suggestive of an altered cytotoxic
110 profile but remaining capacity for tumor cell killing. CXCL13 was a common marker of PD-
1^{high}CD8⁺ and PD-1^{high}CD4⁺ T cells. We also found that sites of B cell and CXCL13^{high} T cell
112 accumulation, but not mature TLS, are more frequent in exhausted immune environments.
Exhausted breast tumor environments were also enriched in cytotoxic CSF-1⁺ natural killer T
114 (NKT) cells and showed evidence of inflammation. Finally, we provide a comprehensive map
of cellular interactions within the breast TIME, revealing strongly elevated immunomodulatory,
116 chemotactic, and cytokine signaling in tumors with an exhausted immune environment.

Our findings suggest that the fundamental differences between the exhausted and non-
118 exhausted immune environments in our study may be explained by different immune escape
mechanisms – avoidance of tumor-specific T cell activation in non-exhausted environments
120 and progressive T cell dysfunction through chronic inflammatory signaling in exhausted
environments. These differences are likely to affect clinical response to different
122 immunotherapies and may explain why PD-L1 blockade has shown limited success so far.
Here, we describe exhaustion-associated TIME characteristics that might facilitate the
124 discovery of new therapeutic targets and propose PD-1, CXCL13 and MHC-I as a new
biomarker combination for patient stratification.

126

RESULTS

128 A single-cell map of immune environments in breast tumors

In order to systematically study the TIME, we performed droplet-based scRNA-seq of 14
130 immune-infiltrated breast tumors (Fig. 1A, top), 12 of which were also included in the cohort
analyzed by Wagner *et al.*²⁹. We selected the tumors based on these previous mass cytometry
132 data. Half of the samples contained exhausted T cells (i.e., PD-1^{high}/CTLA-4^{high}/CD38^{high} T
cells); we annotated these as immune environment 1 (IE1). The other half mainly contained T
134 cells that did not express exhaustion markers and were annotated as immune environment 2

136 (IE2). With one exception, all tumors analyzed by scRNA-seq were classified as luminal (S1A, left). Although all tumor grades were represented, most tumors were of grade 3 (S1A, right).

138 We subjected live, dissociated cells with no cell type enrichment to single-cell transcriptome sequencing using the 10x Genomics platform. After standard data pre-processing, 119,000 high-quality cell measurements remained in the dataset (Fig. S1B), and no batch effect was apparent for individual tumors (Fig. 1B) or immune environments (Fig. 1C). We manually annotated graph-based clusters (Fig. S1C) based on differential expression analysis and known marker genes for the main expected cell types (Fig. 1D-1E, Fig. S1D). This revealed 142 36,000 T and NK cells, which clustered together due to their transcriptional similarity; 27,000 cells belonging to the myeloid lineage (monocytes, macrophages and DCs, excluding granulocytes); and 18,000 epithelial cells. Other cell types were present at lower frequencies. 144 We did not recover adipocytes and neutrophils, likely because they are particularly vulnerable to sample processing and cryopreservation damage^{30,31}. We observed few significant differences in frequencies of the main cell types between tumors with IE1 versus IE2 (Fig. 1F). 146 Importantly, although different T cell phenotypes drove the distinction between IE1 and IE2, the overall T cell frequency was similar in both groups. 150

152 To understand our scRNA-seq based findings in the *in situ* tumor context, we performed IMC on formalin-fixed, paraffin embedded (FFPE) tissue of 12 of the 14 sequenced samples (Fig. 1A, bottom). For each sample, two consecutive FFPE sections were stained with two different panels of antibodies and/or mRNA probes (Fig. S2A, Fig. S12, Fig. S13): Panel 1 (the Protein Panel) consists of 42 metal-labeled antibodies, and Panel 2 (the RNA Panel) includes 12 oligonucleotide probes²⁴, the majority targeting cytokine mRNAs, and 26 antibodies. The marker choice for both panels was informed by analysis of the scRNA-seq data. Prior to IMC, 156 we used whole-slide immunofluorescence imaging of cell type markers to select four to six regions of interest (ROIs) representative of the general tissue structure. For samples that had 158 immature or mature TLS (defined as sites of B cell accumulation without a clear center or sites with dense round B cell accumulation, respectively³²), additional regions including these structures were imaged (Fig. S2B). In total, we acquired 77 ROIs for each panel (Fig. 1G), and data pre-processing and single-cell segmentation resulted in more than 400,000 single cells per panel, with manually matched ROIs for consecutive slices having similar cell numbers (Fig. S2C). We performed graph-based clustering based on average marker expression to 162 identify the cell types present (Fig. 1H, Protein Panel: Fig. S2D-S2G, RNA Panel: Fig. S3A-S3C). All cell types identified in the scRNA-seq dataset as well as neutrophils were identified in our IMC dataset; neutrophils were generally rare but were present at slightly higher frequency in IE1 samples than in IE2 samples (Fig. S2H). For the RNA Panel IMC dataset, we 170 assigned a binary cytokine expression status to each cell based on the signal intensity for the given cytokine corrected by that of a background mRNA probe complementary to the bacterial *DapB* mRNA. These data were then used for a comprehensive, spatially resolved, immune-focused analysis of the tumor microenvironment. 172

174

176 **PD-1^{high}/CTLA-4^{high} T cells are tumor-reactive, proliferative, and coincide with high MHC-I expression in tumor cells**

178 Expression of T cell exhaustion markers at the protein level is the most distinguishing feature
of the two immune environments IE1 and IE2 in our study cohort. To further probe the T cell
180 functional states in these tumors, we analyzed the transcriptomes of T cell subtypes. We also
included NK cells in this analysis, since these cells have transcriptional and functional
182 similarities with T cells and can reportedly undergo exhaustion³³. We first used a pseudobulk
approach, averaging read counts across cells for individual patient samples. This identified
184 several genes expressed at higher levels in IE1 than IE2, including transcripts *PDCD1*,
CD276, and *HAVCR2* encoding immune checkpoint receptors PD-1, B7-H3, and Tim-3,
respectively (Fig. 2A), as expected from our previous mass cytometry data²⁹. A number of
186 genes normally associated with T cell activation, such as *MKI67* (encoding Ki-67) and *GZMB*
(encoding Granzyme B), were also expressed at higher levels in IE1 than IE2 (Fig. 2A). In
188 addition, mRNAs encoding three transcription factors (IRF4, BATF4, and TOX) previously
associated with strong and/or chronic TCR signaling^{34–36} were expressed at significantly higher
190 levels in T and NK cells from IE1 than from IE2 (Fig. 2B). In contrast, *TCF7*, which encodes a
transcription factor positively associated with favorable response to checkpoint therapy in
192 melanoma³⁷, was elevated in IE2 compared to IE1. Finally, we found that cytokine and
cytokine receptor expression was generally higher in T and NK cells from IE1 than from IE2,
194 with the most significant differences seen for *CCL3*, *CXCR6*, *CSF1*, and *IL13*, all of which
have roles in inflammatory signaling (Fig. 2C). Running the same analysis while accounting
196 for tumor grade gave similar results (Fig. S11A).

To compare the phenotypic composition of the T and NK cell compartment in the IE1 and IE2
198 immune environments, we performed graph-based subclustering of the scRNA-seq data and
annotated cellular subtypes based on differential expression analysis. This revealed 14 T cell
200 clusters, four NK cell clusters, and one NKT cell cluster (Fig. 2D-2F, Fig. S4A-C). We identified
a T_{reg} cluster as well as a naïve T cell cluster based on canonical marker expression
202 (*FOXP3/IL2RA* and *CCR7*, respectively). In addition to a CD8⁺ exhausted T cell cluster (T-
CD8-exhausted) annotated based on expression of exhaustion markers (e.g., *PDCD1* and
204 *LAG3*) and enriched in IE1 (Fig. 2E), we identified four CTL clusters: T-cytotoxic-1, 2, and 4
(Fig. S4D), were present in similar proportions in IE1 and IE2. T-cytotoxic-3 was significantly
206 more frequent in IE2 environments (Fig. 2E), and overexpressed early activation (*CD69*) and
cytotoxicity-mediating mRNAs (*TNF*, *GZMK*, *GZMA*) in addition to mRNAs encoding a range
208 of ribosomal proteins and the main TCR components (*CD3D*, *CD3G*, *CD3E*, *TRAC*), hinting
at weak or transient TCR engagement of these cells^{38,39}. We further identified two *CD4*^{high} T
210 cell clusters enriched in IE1 that highly expressed *PDCD1* along with known markers of T
follicular helper (Tfh) cells (clusters Tfh-1 and Tfh-2)⁴⁰. Finally, four T cell clusters (T-mixed-1
212 to 4) contained both CD4 and CD8 cells (Fig. S4E) and showed no IE-specific enrichment. We
identified two more IE1-enriched clusters: an NKT cell cluster that co-expressed *CD3E* with
214 classical NK cell markers such as *NCAM1*, *NCR1*, and *KLRC1* (Fig. 2E-2F, Fig. S4F) and a
proliferating cell cluster (T-proliferating) that highly expressed *MKI67* along other cell division
216 genes. Enrichment of individual clusters in IE1 or IE2 was not driven by differences in tumor
grade (Fig. S11B). Our scRNA-seq analysis was largely confirmed by the IMC data, where we
218 also identified T_{regs}, NK cells, CD8⁺/PD-1^{low}, CD8⁺/PD-1^{high}, CD4⁺/PD-1^{low}, and CD4⁺/PD-1^{high}
metaclusters (Fig. S5A-S5C), with CD8⁺/PD-1^{high} and CD4⁺/PD-1^{high} T cells enriched in IE1
220 tumors (albeit not significantly when considering the IMC data alone, Fig S5C).

Next, we explored exhaustion-associated phenotypic T cell states in more detail. T cell
222 exhaustion has been described as a continuous process during which self-renewing progenitor

224 cells express the transcription factor TCF7, which is then gradually lost with increasing
exhaustion and decreasing proliferation potential⁴¹. We indeed observed reduced expression
226 of *TCF7* mRNA in IE1 (Fig. 2B) and specifically in the IE1-enriched T-CD8-exhausted cluster
(Fig. 2E, 2G), although this could not be observed at the protein level in IMC (Fig. S5D).
228 However, IE1 environments are also enriched in proliferating T cells compared to IE2 (Fig.
2E), and IMC analysis confirmed elevated Ki-67 expression in the PD-1^{high} T cell subsets (Fig.
S5E). Additionally, we found that the IE1-enriched T-CD8-exhausted cluster expressed higher
230 levels of many transcripts that distinguish tumor-reactive T cells from bystander T cells (which
do not experience TCR signaling from the tumor and can be included in the naïve or cytotoxic
232 clusters)^{41,42} when compared to other CD8⁺ T cell clusters (Fig. 2G). These include transcripts
encoding CD39 (*ENTPD1*), CD103 (*ITGAE*), inhibitory receptors like PD-1 (*PDCD1*), LAG-3,
234 Tim-3 (*HAVCR2*), and CTLA-4, T cell activation markers such as 4-1BB (*TNFRSF9*) and GITR
(*TNFRSF18*), and the B cell chemoattractant CXCL13. The T-proliferating cluster was also
236 enriched in all tumor reactivity- and exhaustion-related transcripts and was low in *TCF7* in
comparison to non-proliferating cells (all other clusters) (Fig. 2H). Taken together, our results
238 indicate that tumor reactivity coincides with CTL exhaustion signatures and that tumor-reactive
T cells remained highly proliferative despite displaying characteristics of exhaustion.

240 We investigated potential sources of the difference in CD8⁺ T cell activation in IE1 and IE2.
Pseudobulk analysis showed that levels of *CD274* mRNA, which encodes the PD-1 ligand PD-
242 L1, were not significantly different between IE1 and IE2 either in the epithelial or in the myeloid
subset (Fig. S4H-S4I), but revealed significantly higher expression of MHC-I-encoding genes
244 in epithelial cells of IE1-classified tumors compared to IE2-classified tumors (Fig. S4H). This
was even more apparent in the IMC analysis, where we observed significantly higher
246 expression of HLA-ABC protein (the main MHC-I complex) on IE1 tumor cells (Fig. 2I). In
contrast, HLA-ABC expression did not differ in high versus low-grade samples in our cohort
248 (Fig. S11C). Our data show that MHC class I expression constitutes a major difference
between IE1 and IE2 tumor cells and show that, at least in this cohort, MHC-I is better
250 associated with CD8⁺ T cell activation than is PD-L1. Whole-slide IHC analysis of CD8⁺ T
cell infiltration for 12 samples used in this study and 13 additional samples from the original
252 Wagner et al. cohort further showed that half of IE1 tumors, but none of the IE2 tumors, were
classified as immune-infiltrated (Fig. S4J). This suggests an association of a “hot” immune
254 phenotype with T cell exhaustion, consistent with previous reports^{43,44}.

Enrichment of antigen-experienced T cells in IE1 was not restricted to the CD8⁺ subset: The
256 frequency of Tfh cells, an antigen-experienced PD-1^{high} CD4⁺ T cell type known to be involved
in B cell maturation and differentiation⁴⁵, was higher in IE1 (Fig. 2E) and strongly correlated
258 with the frequency of CD8⁺ exhausted T cells (Fig. S4K). Tfh frequency was also correlated
with plasma cell but not B cell frequency (Fig. S4K), indicating that Tfh cells might act as
260 mediators of B cell differentiation into plasma cells in this context. In line with previous reports,
both the T-CD8-exhausted and Tfh cell clusters in our dataset express *CXCL13* (Fig. 2E-G),
262 and expression of *CXCL13* and *PDCD1* correlated across clusters and across patients (Fig.
S4L and S5G). Elevated *CXCL13* expression in IE1 was confirmed in IMC on both transcript
264 and protein levels (Fig. 2J-2K) and the proportions of CXCL13⁺ T cells measured by scRNA-
seq and IMC on two separate pieces of the same tumor were highly correlated (Fig. S5F),
266 indicating that CXCL13⁺ T cell frequency is a tumor-wide characteristic. Our data suggest that
CXCL13⁺ T cell frequency better distinguishes the IE1 and IE2 environments than frequency
268 of PD-1^{high} T cells (Fig. 2K, compare Fig. S5C) and this difference could not be explained by

270 tumor grade (Fig. S11D). Taken together, these findings indicate that T cells in the exhausted
272 immune environment are proliferative, show a tumor-reactive signature and, despite signs of
terminal T cell exhaustion, might retain more anti-tumor activity than T cells in tumors with a
non-exhausted immune environment.

274 **Cytotoxic potential in exhausted immune environments is altered but not abolished**

276 Next, we examined how the two immune environments differ in T and NK cell cytotoxic
potential, focusing on the main molecules involved in CTL-mediated target cell killing.
278 Pseudobulk comparison of nine selected genes in IE1 versus IE2 samples revealed that the
only cytotoxic molecule significantly elevated in the IE2 T and NK cell compartments was *TNF*,
and that *GZMB*, *GNLY* (encoding Granulysin), and *FASL* (encoding Fas ligand) were
280 overexpressed in IE1 (Fig. 3A). *GZMB* was amongst the top differentially expressed genes
(Fig. 2A), and we also observed a trend towards elevated Granzyme B protein expression in
282 CTLs from IE1 tumors with IMC (Fig. S6A). *GZMB* and *FASL* expression were highest in the
T-CD8-exhausted cluster (Fig. 3B), indicating that these T cells have the potential to exert
284 cytolytic effector functions despite their exhausted phenotype. Their cytotoxic profile is,
however, different from that of the other CTL clusters, especially T-cytotoxic-1 which highly
286 expresses the classical cytotoxicity-related cytokines *IFNG* and *TNF*.

288 In order to assess whether the difference in cytotoxic potential between IE1 and IE2 can be
better described in the context of a gradual exhaustion process, we placed the single-cells of
our CD8⁺ T cell subsets on a linear pseudotime trajectory. We used a Bayesian approach
290 called Oujia⁴⁶, which performs pseudotime ordering upon input from a given set of markers, in
our case levels of transcripts associated with T cell activation or dysfunction (Fig. S6B). The
292 output was a trajectory with naïve T cells on one end and exhausted T cells on the other, with
the cytotoxic clusters intermediate (Fig. 3C-3D). The clusters previously identified as
294 transition/early activation phenotypes (T-cytotoxic-3 and -4, Fig. 2) had lower pseudotime
scores than the other cytotoxic clusters, supporting the validity of our pseudotime ordering
296 (Fig. 3D). Not surprisingly, mean pseudotime scores were higher for IE1-classified samples
(Fig. 3E), but there was substantial variability within the individual IE groups, supporting the
298 notion of immune exhaustion as a continuum and suggesting that the T cells in the IE1
samples are further along this continuum.

300 We examined gene expression profiles over pseudotime to identify early- and late-exhaustion-
genes, associated with IE2 and IE1, respectively. We discovered that *CXCL13*, *CTLA-4*, and
302 *PD-1* had the sharpest increases at the late exhausted stage (Fig. S6B). *LAG-3* and *TIGIT*
displayed a more gradual increase, which also began relatively early in the pseudotime
304 course. Among the cytotoxic genes, we observed an early increase of *IFNG* and *TNF*, closely
followed by *GZMB*; but these three markers subsequently followed different trajectories (Fig.
306 3F). *GNLY* expression was significantly increased in IE1 versus IE2 in pseudobulk analysis
(Fig. 3A) and had a pseudotime profile with a peak in the middle and a decrease in the late
308 stages. The main source of *GNLY* expression within the T and NK cell compartments were
NKT cells (Fig. 3B, S4F), a strongly cytotoxic cell type with a poorly understood role in human
310 cancer⁴⁷.

312 To better understand how NKT cells might act on the IE1 environment, we examined their
expression profile in more detail. One of the few uniquely overexpressed genes in the NKT
cell cluster was *CSF1* (Fig. 3G), which encodes a cytokine important for the activation and
314 differentiation of myeloid cells⁴⁸. We used this marker to annotate NKT cells in our IMC
dataset, defining CSF-1⁺ T and NK cells as NKT cells and confirming the overrepresentation
316 of this cell type in IE1 environments at the protein level (Fig. S6C).

Thus, the main effectors of T and NK cell-mediated cytotoxicity appear to be distinct in the two
318 immune environments. Our data indicate that the T cells in IE1 and IE2 samples are present
in an exhaustion continuum, and that IE1 T cells are further along this continuum than those
320 in IE2. The exhausted-like immune environment IE1 is characterized by strong upregulation
of *GZMB* in exhausted T cells and the presence of *GNLY*-expressing NKT cells, suggesting
322 cytotoxic potential. The previously unreported expression of CSF-1 by NKT cells in exhausted
immune environments may represent a link between T cell activity and myeloid-cell mediated
324 immune responses.

326 **Myeloid cells in exhausted immune environments indicate increased inflammation**

We went on to explore in more detail how different myeloid cell subsets might affect T cell
328 state and disease progression in IE1 and IE2. We first performed pseudobulk analysis on the
myeloid cell fraction (monocytes, macrophages and DCs, excluding granulocytes) to compare
330 the two IEs (Fig. 4A). Several cytokine-encoding mRNAs were overexpressed in IE1 (Fig.
S7A), most notably *CCL18*, which has previously been associated with breast cancer
332 metastasis⁴⁹. We also observed overexpression of genes encoding major complement system
components in IE1 compared to IE2 (Fig. *S7A*), indicating higher inflammatory and phagocytic
334 potential of IE1 myeloid cells. In IE2-classified tumors, we observed upregulation of *CD55* and
CD46, which encode proteins that limit complement function⁵⁰, in T and NK cells (Fig. *S7B*).
336 Finally, there was increased expression of transcripts encoding matrix metalloproteinases,
implicated in breast cancer invasion and metastasis⁵¹, and of metallothioneins, which protect
338 cells from oxidative stress and cytotoxicity, in IE1 myeloid cells (Fig. *S7A*). Running the same
analysis while accounting for tumor grade revealed a similar trend (Fig. S11E). Taken
340 together, these data are indicative of inflammation in IE1 tumors.

Graph-based subclustering of the scRNA-seq profiles from the myeloid cell fraction revealed
342 two clusters of monocytes or early differentiating macrophages (mono-1 and mono-2), seven
clusters of TAMs, five clusters of DCs, and one cluster of proliferating myeloid cells (Fig. 4B,
344 Fig. *S7C*). All patient samples contained monocytes, TAMs, and DCs (Fig. *S7D*), although
three out of the seven TAM clusters were found mainly in one patient sample each (Fig. *S7E*).
346 Most monocyte and TAM clusters tended to be more frequent in IE1 tumors without any
individual cluster reaching significance (Fig. 4C), whereas IE2 tumors showed enrichment of
348 one specific TAM cluster (cluster TAM-2) as well as classical DCs type 2 (cluster cDC2).
Enrichment of cDC2 in IE2 was not driven by differences in tumor grade (Fig. S11F).

350 A closer survey of differentially expressed genes in the identified subclusters revealed a
monocyte-specific gene signature for cells of the mono-1 cluster. The mono-2 cells showed
352 patterns also overlapping with several TAM clusters and likely represent a transition
phenotype from monocyte to mature macrophage (Fig. 4D). TAM clusters showed high

354 expression of *CD68*, *CD163*, *MRC1* (also known as *CD206*), and *MSR1* (also known as
356 *CD204*) (Fig. S7F). TAM-1 and TAM-2 cluster phenotypes were similar, both highly expressed
358 cytokine-encoding mRNAs such as *IL10*, *CCL3*, *CCL4*, and *CXCL8* with the TAM-1 cluster
360 cells additionally high in *TNF*. Conversely, the TAM-3 cluster was unique in its high expression
362 of mRNAs encoding T cell-attracting chemokines *CXCL9*, *CXCL10*, and *CXCL11* as well as a
range of interferon-induced genes. TAM-4 and TAM-5 clusters were fully mature macrophage
subsets, co-expressing *MRC1*, *MSR1*, and *SIGLEC1* (also known as *CD169*) but
comparatively low in cytokine expression. Finally, TAM-6 and TAM-7 clusters were both
dominated by cells from the same patient (TBB338) and each displayed a unique
transcriptional profile.

364 Having observed exhausted T cells and signs of inflammation and myeloid cell differentiation,
we next examined crosstalk of the different immune compartments. We quantified T cell-
366 attractive and T cell-suppressive properties of myeloid cells using gene signatures that we
assembled from the literature (Genes: Supplementary Table S5). We were able to functionally
368 validate the T cell attraction signature and a subset of markers within the T cell suppression
signature using spatial IMC analysis (Fig S7G-S7H). The two signatures showed a positive
370 correlation at the single-cell level (Fig. S7I), at the patient level (Fig. S7J), and at the level of
phenotypic clusters (Fig. 4E), suggesting that myeloid cells that harbor a strong suppressive
372 potential might also actively attract T cells. Most TAM clusters showed high scores for both
signatures, whereas monocyte and DC clusters tended to have low scores. Both signatures
374 tended to be enriched in IE1 tumors compared to IE2 tumors, as were gene signatures for
“classically activated” (M1) and “alternatively activated” M2 macrophages²⁷ (Fig. S7K-S7L).
376 This confirmed an overall higher activation and differentiation state of myeloid cells in IE1
environments than in IE2 tumors.

378 Apart from cDC2s, which represent the most frequent DC subset in our cohort and are strongly
enriched in IE2, we were able to distinguish four other DC subsets previously described in
380 human breast tumors⁵² (Fig. 4D). Classical DCs type 1 (cluster cDC1), Langerhans cells
(cluster LC) and plasmacytoid DCs (cluster pDC) were identified based on their high
382 expression of *CLEC9A*, *CD207*⁵² and *IRF7/PLAC8/IL3RA*, respectively. A fifth DC subset
showed elevated expression of *LAMP3*, *FSCN1*, and *CCR7* and was identified as migratory
384 DCs (migDCs) as described recently in healthy thymus and various cancer types including
breast^{15,53–55}. The migDC cluster displayed a particularly strong T cell-suppression signature
386 compared to other DCs (Fig. 4E). We found that this cell type displayed the highest expression
of *CD274* (which encodes PD-L1) not only in the myeloid compartment but in the entire TIME
388 (Fig. 4F and Fig. S8A). It was also the main producer of the *PDCD1LG2* mRNA, which
encodes PD-L2, the second known PD-1 ligand. The migDCs also expressed *IDO1*, *CD80*,
390 and *CD40* and exhibited a unique cytokine expression profile with high counts of *CCL17*,
CCL19, *CCL22*, and *IL15*, which were not detected in other myeloid cell subsets. In our IMC
392 dataset, we confirmed high levels of co-expression of PD-L1, IDO1, and CD40 proteins and
CCL17 and *CCL22* transcripts with the migDC marker *LAMP3* (Fig. S8B, C). In summary, the
394 expression profile of migDCs suggests the potential to recruit immune cells and to strongly
contribute to T cell suppression.

396 Given that the abundance of migDCs did not differ between IE1 and IE2, we wanted to
understand whether there was a difference in the DC transitional continuum. Different primary
398 DC subsets have the potential to become migDCs^{54,56}. Slingshot trajectory inference analysis

of our data implied the existence of a transitional state between cDC2s and migDCs, consistent with previous work suggesting that most migDCs in human tumors originate from cDC2 cells^{55,57}; the cDC1 subset clustered apart (Fig. 4G). Using Monocle2 for trajectory inference gave similar results (Fig. S8D). We observed distinct expression dynamics of the migDC markers such as *CCL17*, *CCL22*, and *CCL19* along the cDC2-migDC transition (Fig. 4H).

In summary, myeloid cells in exhausted and non-exhausted immune environments differed in inflammatory cell states, and we observed evidence of crosstalk between myeloid cells and T cells. In addition, we have identified a LAMP3+ migratory DC subset that likely originates from cDC2 cells and displays a particularly high T cell-suppressive potential.

410 Immune states are linked to distinct cell-to-cell communication patterns

We then investigated systematically how cellular crosstalk differs in the IE1 and IE2 immune environments by performing cell type interaction analysis using SingleCellSignalR, an algorithm that infers intercellular networks from single-cell transcriptomic data based on a manually curated ligand-receptor database⁵⁸. We first quantified the total number of predicted ligand-receptor interactions for each cell type pair across all samples (Fig. 5A, Fig. S9A). This revealed many predicted interactions between fibroblasts and endothelial cells and myeloid cell auto-interactions. T cells, B cells, and plasma cells were generally predicted to have a lower number of interactions, partly explicable by the overall fewer expressed genes in these cell types. Analysis with a second algorithm for inference of cellular crosstalk, CellPhoneDB, confirmed these trends (Fig. S9B). To separate cell type-specific from ubiquitous interactions, we used the score coefficient of variation of the 100 top-scoring predicted ligand-receptor interactions for each of the main cell type pairs to identify pair-specific interactions (Fig. S9C). We found that, for example, fibroblast-to-endothelial interactions were dominated by collagens and integrin receptors, whereas specific myeloid-to-T cell crosstalk involved interactions of several cytokines with their cognate receptors.

We next compared predicted interactions in exhausted versus non-exhausted breast tumor immune environments. We applied SingleCellSignalR to data from each patient individually (focusing on epithelial, myeloid, and T and NK cell interactions) and found a number of predicted ligand-receptor pairs enriched in either IE1 or IE2 tumors (Fig. 5B). As expected, many predicted immunomodulatory interactions such as *CD274* with *PDCD1* (at the protein level, PD-L1 with PD-1), *CD80* with *CTLA-4*, *LGALS9* with *HAVCR2* (at the protein level, Galectin-9 with Tim-3), and *PVR* with *TIGIT* were enriched in IE1 tumors, with mRNAs encoding the ligands for PD-1 and CTLA-4 expressed at significantly higher levels only by myeloid cells. IE1 tumors also had increased scores for chemotactic interactions, mainly mediated by *CCL3*, *CCL4*, *CCL5*, and *CXCL9*, suggesting the presence of a more dynamic immune environment with increased recruitment of cells from outside the tumor. Furthermore, several predicted non-chemotactic cytokine interactions were enriched in IE1 tumors, some activating (CSF-1 and IL15 with respective receptors), and others with more complex predicted functions (e.g., IL10 with its receptor). The only predicted cytokine interaction enriched in IE2 tumors was that of *FLT3* ligand, a stimulator of DC growth⁵⁹ and expressed by T and NK cells and its receptor on myeloid cells. Other interactions enriched in IE2 tumors included those of

442 ERBB4 and of thrombospondin with their ligands. Performing a comparable analysis with
CellPhoneDB yielded similar results (Fig. S9D).

444 To examine how specific myeloid cell subtypes and T and NK cell subtypes found in exhausted
and non-exhausted environments may interact with each other, we repeated the interaction
446 analysis focusing only on these subtypes (Fig. 5C). For better biological interpretability, we
first aggregated the identified clusters into larger metaclusters, each representing a specific
448 cellular subtype. All T and NK cell and myeloid metacluster pairs had between 300 and 600
predicted interactions, with TAM auto-interactions the most frequent. With the exception of
450 migDCs, cell types with many outgoing interactions (i.e., the cells express the ligand) also had
many incoming interactions (i.e., the cells express the receptor). Predicted ligand-receptor
452 interactions that were specific for certain metacluster pairs (Fig. S9E) included the interaction
between Tfh cell-specific IL21 and IL13 with respective receptors on myeloid clusters, the
454 interaction between CCL18 and CCR8 (on TAMs and T_{regs}, respectively) and that of CCL17
and CCL22 (expressed by migDCs and cDC2s) with CCR4 (expressed predominantly by T_{regs}
456 and Tfh). As a next step, we wanted to predict which myeloid-derived ligands are the most
closely linked to T cell exhaustion. For this purpose, we applied NicheNet, a method that does
458 not directly look at ligand-receptor interactions, but instead builds upon prior knowledge on
signaling networks to predict which ligands of the sender cells (in our case, myeloid cells) are
460 most likely to have affected the expression of a set of known target genes (in our case, CD8+
T cell exhaustion-related genes) in the receiver cells. The myeloid-derived ligand that was
462 identified by NicheNet to best predict expression of exhaustion-related genes was IL15,
followed by IL1B and CXCL16 (Fig. 5D). This is consistent with the fact that the IL15-IL15
464 receptor interaction is enriched in IE1 tumors compared to IE2 tumors (Fig. 5B, S9D). The
main producer of IL15 are migDCs (Fig. 4F), providing yet another link between migDCs and
466 T cell exhaustion.

In conclusion, ligand-receptor analysis provided a comprehensive quantitative map of
468 potential interactions across breast cancer TIMEs. We report an enrichment of T cell-
regulatory interactions and enhanced cytokine and chemokine signaling in IE1, especially from
470 myeloid cells to T and NK cells, compared to IE2, suggesting a balance of ongoing immune
cell recruitment and regulation in exhausted environments.

472

Spatial distribution of immune cells varies with exhaustion

474 Ligand-receptor analysis can predict intercellular communication, but it is blind to an important
requirement for cellular interaction: spatial proximity. Therefore, we sought to use our IMC
476 data to examine the spatial distribution of cell types and ask whether cells that are predicted
to interact based on their ligand and receptor expression patterns are also physically close to
478 each other in the tissue, and whether spatial patterns differ in IE1 and IE2.

We used pairwise neighborhood analysis to quantify relative avoidance or interaction for each
480 cell type pair (accounting for cell type frequency)⁶⁰ and found that fibroblasts and endothelial
cells were strongly enriched in each other's neighborhood (Fig. 6A) (rectangle #1), consistent
482 with predicted ligand-receptor interactions between the two (Fig. 5A). Similarly, spatial
analysis is consistent with predicted myeloid cell auto-interactions (rectangle #2). As expected,
484 tumor cell subtypes formed a spatial cluster (rectangle #3) and tended to avoid other cell types.

486 However, some tumor subtypes did show spatial proximity to other cell types: hypoxic and
apoptotic tumor cells had a higher likelihood of neighbouring immune cells (rectangle #4) and
PD-1^{high} T cells were more likely to border tumor cells than PD-1^{low} T cells (rectangle #5). We
488 also observed spatial patterns within immune cell types. Myeloid cells, T_{regs}, CD4⁺ T cells, and
CD8⁺ T cells formed a spatial cluster (rectangle #6), as did PD-1^{high}/CD8⁺ T cells, PD-
490 1^{high}/CD4⁺ T cells, and migDCs (rectangle #7).

Overall, we observed that PD-1^{high} T cells were significantly more likely to have at least one
492 migDC as their direct neighbor compared to PD-1^{low} T cells (Fig. 6B-C). This is consistent with
the predicted PD-1-PD-L1 interaction between myeloid and T cells identified in our ligand-
494 receptor analysis and with the finding that migDCs are the main producer of PD-L1 in our
samples. Our data thus suggest direct engagement of PD-L1-expressing migDCs with PD-1-
496 expressing T cells. To further examine exhaustion-associated spatial motifs, we quantified cell
type composition of the immediate neighbourhood (10 closest neighbours) of different T cell
498 subtypes in non-TLS images. This revealed that, on average, PD-1^{high} T cells were surrounded
by fewer myeloid cells and fibroblasts, but by more other PD-1^{high} T cells, pDCs and migDCs,
500 when compared to PD-1^{low} T cells and Tregs (Fig. 6D).

Pairwise neighbourhood analysis did not reveal major differences between the relative
502 interaction or avoidance of cell type pairs in IE1 compared to IE2 (data not shown), but IMC
analysis showed a more than 5-fold higher proportion of cytokine-expressing cells in IE1 than
504 in IE2 tumors (Fig. S10A). We observed this increase for every cell type but especially for T
and NK, SMA⁺ stromal cells, and myeloid cells (Fig. S10B). In addition, a large proportion of
506 cytokine-expressing cells in IE1 but not IE2 tumors were part of a cytokine patch (defined as
a spatial cluster of at least three cytokine-expressing cells directly neighboring each other)
508 (Fig. S10C). In order to identify the cell types surrounding these patches across the whole
cohort, we defined cytokine milieus comprising all cells within a radius of 30 μm from a given
510 cytokine patch and looked at the enrichment of cell types in these milieus compared to the
overall tissue (Fig. 6E). We found that CD4⁺ T cells were enriched in *CXCL9*, *CCL22* and
512 *CXCL13* milieus, whereas CD8⁺ T cell enrichment was highest in *CXCL9* and *CXCL10* milieus
(Fig. 6F, top). As expected, B cells were strongly enriched in *CXCL13* milieus, and migDCs
514 were enriched with *CCL17* and *CCL22* milieus. Finally, myeloid cells were enriched in *CCL18*
milieus (Fig. 6F, bottom) and tumor cells were depleted across most cytokine milieus. Thus,
516 we conclude that spatial cytokine expression patterns are linked to cell type distribution and
exhaustion state of the immune environment.

518 One of the most distinct structural elements found in solid tumors are TLS, which differ
considerably from the surrounding tissue in terms of cell type frequency and spatial
520 distribution⁶¹. Our transcriptomics data showed higher frequency of Tfh cells and lower
frequency of B cells in IE1 versus IE2 tumors, and was therefore contradictory for the likelihood
522 of TLS being present in these two groups (Fig. S4L). To directly examine TLS in both immune
environments, we acquired immunofluorescence whole-slide scans of 13 samples from the
524 original Wagner et al. cohort and from 12 samples used in this study. We found that densely
packed, mature TLS were more frequent in IE2-classified tumors, whereas immature TLS (see
526 methods for criteria, and Figure S2B) were more frequent in IE1-classified tumors (Fig. 6G).
In IMC images, we found that most immune cell types were enriched in images containing
528 TLS compared to images that do not contain TLS and that there were only minor differences
between immune cell frequencies in images that contained immature versus mature TLS (with

530 the exception of B cells, which are highest in mature TLS as expected⁶¹) (Fig. S10D). Although
the frequencies of *CXCL13*⁺ T cells, which reportedly play a large role in TLS formation⁶², did
532 not differ significantly between images with immature versus mature TLS (Fig. S10E), the
spatial distribution of these cells changed: Most *CXCL13*⁺ T cells in images containing mature
534 TLS were part of a *CXCL13*-cytokine patch, the opposite was true for immature TLS images
(Fig. 6H). Neighbourhood analysis on images containing mature or immature TLS further
536 revealed an enrichment of direct PD-1^{high} T cell-migDC interactions in these images compared
with the full dataset (Fig. S10F).

538 In conclusion, spatial analysis was consistent with major predicted intercellular interaction
axes and revealed that spatial clusters of cytokine-expressing cells were frequent in IE1 but
540 not IE2 tumors. In addition, our data suggest that migDC-mediated regulation of T cell activity
occurs via direct interactions that take place preferentially in regions of mature and immature
542 TLS and that tumors with different immune environments differ in the spatial distribution of
CXCL13⁺ T cells.

544

DISCUSSION

546 Despite having a better prognosis than triple-negative and HER2⁺ tumors, the majority of
patients who die of breast cancer have tumors of the Luminal subtype due to its high
548 incidence⁶³. Immune-checkpoint therapy regimes for Luminal B tumors are currently being
evaluated in clinical trials but have not been approved⁶⁴. To better understand the responses
550 of breast cancer patients to immune modulators, we have performed detailed transcriptomic
and spatial proteomic characterization of distinct breast tumor immune environments at single-
552 cell resolution. These analyses revealed systematic changes in the exhausted-like
environment associated with chronic T cell stimulation. We found that the presence of a PD-
554 1^{high} exhaustion-like T cell phenotype was indicative of an inflamed immune environment with
altered cytotoxic potential, cellular composition, and intercellular crosstalk.

556 scRNA-seq analysis revealed that in CD8⁺ T cells that express markers of exhaustion,
hallmark genes of tumor-reactive T cells are upregulated, consistent with results in other tumor
558 types⁴². Strikingly, expression of MHC-I transcripts in tumor cells in IE2-classified tumors,
which have few exhausted-like T cells, was substantially lower than in IE1-classified tumors.
560 MHC-I downregulation is one mechanism by which tumor cells escape immune surveillance⁶⁵,
and our data suggest that downregulation of this complex could explain the reduced tumor
562 reactivity of T cells in IE2 tumors. It has been shown that in a cohort of anti-PD1 treated breast
tumor patients, low pre-treatment expression of MHC-I on tumor cells was associated with
564 reduced T cell expansion on treatment¹⁵. Thus, we hypothesize that this form of immune
evasion, observed in IE2 but not IE1 tumors, is not amenable to conventional immune
566 checkpoint therapy. Immune evasion of IE1 tumors, on the other hand, is linked to chronic
stimulation and a progressively exhausted phenotype of tumor-reactive T cells and may be
568 targetable by immune checkpoint blockade. Despite rigorous method validation and carefully
considered cohort selection, our study has limitations: First, we did not study the third tumor-
570 immune group identified in Wagner et al.²⁹ (representing 31% of all tumors), as this group
had generally low cell numbers after dissociation, a small immune proportion, and few T cells
572 compared to the other two groups. Second, the small size and low number of cells obtained

574 from most breast tumors made additional experiments such as ex vivo validation of T cell
cytotoxicity impossible. Third, histological tumor grade is a co-variate that is not perfectly
576 balanced in our cohort. However, we found that the characteristics that differed most
significantly between IE1 and IE2 showed no difference between low-grade and high-grade
578 tumors in our cohort, and that accounting for grade in pseudobulk analysis did not substantially
change the observed differential expression pattern.

580 Positive correlation of the exhausted-like CD8⁺ T cell proportion with that of an antigen-
experienced CD4⁺ T cell subset (Tfh) indicates that the extent of tumor antigen exposure is
582 similar for CD8⁺ and CD4⁺ T cells despite different antigen recognition mechanisms. Since
DCs may cross-present tumor antigens to both CD8⁺ and CD4⁺ T cells, this suggests that
584 differential MHC-I expression by tumor cells is not the only reason for higher T cell stimulation
in IE1-classified tumors. Indeed, transcripts for a number of antigens such as CTAG2,
586 MAGEA3, and MAGEA6, which are normally expressed in testis and are immunogenic when
aberrantly expressed in cancer tissue, are strongly expressed in a subset of IE1, but not IE2,
588 samples (Supplementary Table S4). Although we do not have quantitative data on tumor
mutational burden or neoantigen load for our cohort, these factors have also been linked to T
cell activation in breast and other cancer types^{62,66,67}.

590 Contrary to the classical notion of T cell exhaustion but in line with findings in other cancer
types^{13,14}, T cells with characteristics of exhaustion in our cohort expressed markers of
592 proliferation. Differential gene expression analysis revealed that the cytotoxic effector potential
of these exhausted-like cells was most probably altered but not abolished, and pseudotime
594 analysis suggested a decrease of *TNF* but an increase of *GZMB* and *FASL* expression during
the progression to T cell exhaustion, indicating a shift in the cytotoxic profile from classical
596 inflammatory cytokines to molecules mediating cytolytic effector functions. In contrast to
reports from other tumor types^{13,14}, we did not observe an increase of IFNG expression
598 associated with T cell exhaustion. The cytotoxic potential of IE1 environments was further
enhanced by the presence of NKT cells, which highly expressed *GNLY* and *GZMA*; these cells
600 were almost absent from IE2 tumors. NKT cell accumulation in exhausted immune
environments has not previously been reported, and its driving mechanism is unknown. In
602 addition to their cytotoxic role, we found that NKT cells might also contribute to myeloid cell
activation and maturation via expression of the cytokine *CSF1*, providing a direct functional
604 link between the lymphoid and the myeloid blood cell lineages. The transcriptional profile of
myeloid cells in IE1 environments revealed more inflammatory phenotypes and stronger signs
606 of surrounding tissue inflammation compared to IE2 environments. This increased tissue
inflammation was accompanied by overexpression of matrix-remodeling metalloproteinases,
608 a phenotype linked to higher risk of metastasis^{51,68}. Thus, although T and NK cells in exhausted
immune environments retain cytolytic capacity, this does not appear to be sufficient to stop
610 disease progression and might even contribute to tumor invasiveness via inflammation-
induced tissue remodeling. The strongly elevated number of cytokine-expressing cells in IE1
612 compared to IE2 tumors observed in IMC provides additional evidence for increased tissue
inflammation in IE1. The tendency of these cells to form spatial clusters, surrounded by milieus
614 with cytokine-specific cell type composition, is also increased in IE1 tumors.

616 We identified a subset of myeloid cells as migDCs; this activated cell type has been described
only recently in healthy thymus and a number of cancer types including breast cancer^{14,15,53,57}.
The predicted role of these *LAMP3*⁺ DCs in the TIME is complex: High levels of cytokine

618 expression by these cells suggests a role in recruitment and activation of other immune cells,
620 but migDCs also have a high T-cell suppressive potential, underlined by high expression of
622 *IDO1* and *CD274* (which encodes the PD-1 ligand PD-L1) and direct spatial interaction with
624 PD-1^{high} T cells. Although PD-L1 expression in the TIME is associated with T cell exhaustion,
626 migDC frequency was comparable in IE1- and IE2-classified tumors. Pseudotime analysis
628 indicated that most migDCs in our cohort originate from cDC2, a cell type significantly enriched
630 in IE2 environments, suggesting the presence of a large pool of potential migDC predecessors
in non-exhausted environments that might counterbalance the expected overrepresentation
of migDCs in exhausted environments. In addition, the migratory phenotype predicted by the
migDC transcriptional profile has been validated in vitro by Zhang et al., who also showed that
migration is lymph-node directed¹⁴. Thus, we speculate that migDCs might not accumulate at
the tumor site but may migrate to the draining lymph node upon full maturation, providing an
explanation for the similar migDC frequencies observed in IE1 and IE2 tumors.

TLS are associated with favorable outcome in many cancer types; however, their prognostic
632 value in breast cancer is unclear⁶⁹⁻⁷³. Our transcriptional and protein-level analyses revealed
634 that antigen-experienced CD8⁺ and CD4⁺ T cells highly expressed the chemokine CXCL13, a
636 B cell attractant essential for TLS formation⁶². Surprisingly, elevated CXCL13 expression in
638 IE1 tumors did not translate into higher frequency of TLS. Instead, we observed more sites of
loosely accumulating B cells and CXCL13⁺ T cells that lacked the dense core typical for TLS
structures and might represent either immature TLS or dissolving structures. Contrary to
mature TLS, where CXCL13⁺ T cells tended to occur in spatial clusters, CXCL13⁺ T cells in
640 these immature sites often were spatially apart from each other. Occurrence of CXCL13⁺ T
642 cells outside of immature or mature TLS was a defining characteristic of IE1 samples. This
suggests that the immune microenvironment of IE1-classified tumors is more dynamic than
that of IE2-classified tumors, with continuing T cell-mediated signals to attract more immune
cells.

644 Cell-to-cell interaction mapping revealed systematic enrichment of immunomodulatory,
chemoattractive, and cytokine signaling in exhausted environments, corroborating the notion
646 that IE1 is a more dynamic immune environment than IE2. Although the focus of our analysis
was on epithelial, myeloid, and T cells, taking advantage of our transcriptomic and spatial data
648 we identified interaction pairs across all cell types in IE1 and IE2 tumors, which provides a
valuable resource for future studies. The endothelial-fibroblast axis with its demonstrated
650 spatial interaction and large number of predicted ligand-receptor pairs will be especially
interesting to explore further.

652 PD-1 expression has previously been associated with poor prognosis in Luminal B tumors⁷⁴,
but because data on disease progression and survival is not yet available for our cohort, the
654 impact of IE classification on patient outcome remains to be confirmed. However, it has
recently been demonstrated that a high abundance of PD1^{high}/CXCL13+ CD4+ and CD8+ T
656 cells, as observed in IE1 tumors, is highly predictive for increased T cell expansion upon anti-
PD1 treatment across all breast cancer subtypes¹⁵ and positively influences response to anti-
658 PD-L1 treatment in triple-negative breast cancer.⁷⁵ Irrespective of prognostic or predictive
value, we have shown that IE1 and IE2 represent two distinct immune environments with
660 respect to tumor antigen presentation, T cell phenotypes, cytotoxic potential, and cellular
crosstalk, all of which are likely to affect immunotherapy response. PD-L1 is currently the main
662 marker used to stratify patients for immune checkpoint therapy in breast cancer⁷⁶. However,

664 our data suggest that PD-1, CXCL13, and MHC-I, possibly along with previously defined T cell
666 exhaustion markers such as LAG-3 and Tim-3²⁹, are better able to distinguish these immune
environments. Thus, we propose that these factors be considered for patient stratification in
upcoming clinical trials.

668 METHODS

Clinical samples

670 Primary breast tumor resectates and health-related data were collected in collaboration with
672 the Patient's Tumor Bank of Hope (PATH, Germany) at the breast cancer centers at St.
674 Johannes Hospital Dortmund and Institute of Pathology at Josefshaus (Germany) and the
676 University Hospital Giessen and Marburg, Marburg site (Germany) after obtaining written
678 informed consent from patients. The majority of patient samples sequenced in this study (12
680 of 14) were originally collected and analyzed by suspension mass cytometry (CyTOF) by
682 Wagner et al.²⁹. For each of these samples, we had access to an aliquot of viably frozen cells
684 derived from the same cell suspension that was used in the original study. These samples
686 were previously classified as either TIG2 or TIG3 by Wagner et al. (corresponding to IE1 and
688 IE2 in this study) based on immune cell subtype frequencies. The remaining two samples
690 (T_BB330 and T_BB338) were collected for this study, and pathological staging was
692 performed by experienced pathologists as previously described²⁹. All tissue and health-related
694 data were collected under approval of the Ethics Committee Zurich (#2016-00215) and the
696 faculty of medicine ethics committee at Friedrich-Wilhelms-University Bonn (#255/06). Part of
each tumor was formalin-fixed and paraffin-embedded for the use in standard diagnostics and
for analysis by IMC. For CyTOF and scRNA-seq analyses, a tissue sample of about 5x5x5
mm was taken prior to paraffin embedding. Thus, the tumor area used for standard diagnostics
and IMC was spatially separate from the tumor area used for mass cytometry and scRNA-
seq. For two out of 14 samples, IMC measurements were not possible due to unsuitable FFPE
material or missing patient consent for FFPE-based analysis. Tumor subtypes in this study
were defined as follows: Luminal A (ER⁺ and/or PR⁺, HER2⁻, Ki-67⁺ < 20%), Luminal B (ER⁺
and/or PR⁺, HER2⁻, Ki-67⁺ ≥ 20%), Luminal B-HER2⁺ (ER⁺ and/or PR⁺, HER2⁺), HER2⁺ (ER⁻,
PR⁻, HER2⁺), and triple negative (ER⁻, PR⁻, HER2⁻). Two out of 14 patients had received
neoadjuvant chemotherapy prior to tumor resection (Supplementary Information, **Table S1 –
clinical data**), but we did not observe any significant difference between tumors from treated
and untreated patients in terms of immune cell type frequency or phenotypes. In the original
Wagner et al. patient cohort, neoadjuvantly treated patients were evenly split between the
three major tumor-immune groups (TIGs)²⁹.

698

Tissue preparation

700 After surgical resection, fresh tissue samples were immediately transferred to pre-cooled
702 MACS Tissue Storage Solution (Miltenyi Biotec) and were shipped at 4 °C. For suspension
704 mass cytometry, the tissue was processed as previously described²⁹. In brief, the Tumor
Dissociation Kit, human and the gentleMACS Dissociator (both Miltenyi Biotec) were used
for tissue dissociation, followed by filtering of the single-cell suspension. Cells were stained

706 for viability with 25 mM cisplatin (Enzo Life Sciences) and subsequently fixed with 1.6%
707 paraformaldehyde (Electron Microscopy Sciences) before storage at -80 °C. For scRNA-seq,
708 an aliquot of the single-cell suspension was taken prior to viability staining and fixation and
709 viable cells were frozen in RPMI-1640 cell culture medium (ThermoFisher) supplemented with
710 10% fetal bovine serum and 10% DMSO (Sigma Aldrich) using a Mr. Frosty Freezing
Container (ThermoFisher). Viable cell aliquots were stored in liquid nitrogen.

712 **Suspension mass cytometry**

713 For the two samples not previously analyzed by suspension mass cytometry, we performed
714 mass tag cellular barcoding, antibody labeling and mass cytometry acquisition as previously
715 described using the same antibody clones (immune-centered antibody panel only)²⁹. Basic
716 data analysis including dimensionality reduction and clustering were performed as described
717 and allowed allocation of each sample to one of the two distinct immune environments
718 explored in this study (based on the frequency of exhausted T cell phenotypes).

720 **scRNA-seq sample preparation, data acquisition and pre-processing**

721 For scRNA-seq, viable cell suspensions were quick-thawed in a 37 °C waterbath for < 1 minute
722 and progressively diluted by slow stepwise addition of RPMI + 10% fetal bovine serum until
723 the volume was 10 times that of the initial volume. After a 10-min centrifugation step (300 g, 4
724 °C), the supernatant was removed and the Dead Cell Removal Kit (Miltenyi Biotech) was used
725 according to manufacturer's instructions to exclude dead and apoptotic cells. The resulting
726 live cell fraction was washed once with 0.04% bovine serum albumin (BSA) in PBS (Sigma
727 Aldrich) and resuspended in the same buffer. Cell quality and cell count were assessed using
728 a Neubauer chamber (Electron Microscopy Sciences), and the concentration was adjusted to
729 800-1000 cells/μl. scRNA-seq libraries were generated using the Chromium Single Cell 3'
730 Library & Gel Bead Kit v3 from 10x Genomics, aiming for 10,000 single cells per library. All
731 libraries were sequenced on a NovaSEQ6000 System (Illumina). Following quality control, raw
732 sequencing reads were aligned to the human reference genome GRCh38 and reads per gene
733 per cell were quantified using Cell Ranger (10x Genomics, v3.0.1) (Supplementary
734 Information, Table **S2 – technical details of the sequencing runs**).

736 **scRNA-seq clustering and cell type annotation**

737 The resulting gene-by-cell matrices from Cell Ranger were transformed into Seurat objects
738 (Seurat v3.0.2)⁷⁷, and downstream analysis was conducted in R v3.6.1 unless otherwise
739 stated. High-confidence doublets were removed using the DoubletFinder package with the pK
740 parameter optimized for each sample individually⁷⁸. Subsequently, all Seurat objects were
741 merged and filtered to exclude cells with >7500 or <200 expressed genes, with >75000 read
742 counts or with >20% of reads mapping to mitochondrial RNA. The remaining cells were
743 normalized and scaled using the *sctransform* wrapper in Seurat⁷⁹. *Sctransform* also identifies
744 highly variable genes, which were then used to construct Principal Components (PCs). PCs

746 covering the highest variance in the dataset were selected based on elbow plots and
748 heatmaps and used as input for graph-based clustering. Clusters were calculated using the
750 FindNeighbours and FindClusters functions with the resolution parameter set to 2 and
752 visualized using the Seurat implementation of the dimensional reduction algorithm UMAP⁸⁰.
754 Differential gene expression analysis was performed for the 61 resulting clusters using the
756 Seurat implementation of the statistical framework MAST⁸¹. The main cell types were
758 annotated based on the expression of established marker genes (*EPCAM/CDH1* for epithelial
760 cells, *CD3/CD4/CD8/NCR1* for the T and NK cell fraction, *CD14/ITGAX/HLA-DRA* for myeloid
cells, *PECAM1/VWF* for endothelial cells, *PDGFRB/FAP* for fibroblasts, *MS4A2* for mast cells
and basophils, *MS4A1* for B cells, and Ig-encoding transcripts for plasma cells)
(Supplementary Information, **Table S3 –full differential expression results and annotation
info for each cluster**). Due to large transcriptional overlaps, T and NK cells could not be
clearly distinguished at this level and were thus annotated as one cell type. No large-scale
batch effects derived from individual patients, sequencing runs or immune environments were
found upon visual inspection of the UMAP. Separate clustering of the epithelial cell fractions
from individual patient samples is biologically expected and not a batch effect.

762 For detailed analysis of immune cell subtypes, 14 clusters identified as T and NK cells and 10
764 clusters identified as myeloid cells were separately subset from the full dataset. Both subsets
766 were re-normalized using *sctransform* while regressing out percentages of mitochondrial RNA
and contaminating ambient RNA (specifically, percentages of keratin-encoding transcripts and
768 percentage of *MGP* likely derived from apoptotic/ruptured epithelial cells) as confounding
770 factors. As for the full dataset, PCs covering the highest variance in each subset were selected
772 and used for graph-based subclustering, which was performed at a range of resolutions
774 between 0.1 and 1.5. The final resolution parameter resulting in stable subclusters at desired
776 granularity was selected using clustering tree analysis⁸² and was 1 for the T and NK cell subset
(Fig. S4A) and 0.8 for the myeloid subset. Low-quality subclusters (one T and NK cell cluster
with high keratin counts, one T and NK cell cluster and one myeloid cluster with very low read
counts, and one myeloid cluster with high mitochondrial percentage) were removed before
performing DE analysis. The most differentially expressed genes for each subcluster were
used for manual cell subtype annotation (**Table S3**). Due to ambiguous *CD4/CD8*
classification of some T cell clusters, we annotated *CD8⁺*, *CD4⁺*, or mixed T cell clusters based
on the ratio of *CD8A* and *CD8B* to *CD4* transcript counts (Fig. S4E).

778

Pseudobulk analysis of scRNA-seq data

780 For pseudobulk comparison of IE1- versus IE2-classified samples, raw gene counts were
782 summed over all cells per sample and normalized by library size for boxplot visualization. This
784 was done separately for the grouped T and NK cells, for the myeloid cells, and for the epithelial
786 cells. Differentially expressed genes were identified using the exactTest for single-factor
experiments from the edgeR package (v3.26.5)⁸³. For this, non-normalized gene-sum matrices
were used as input, lowly expressed genes were filtered out (cutoff: >30 read counts in at least
3 samples) and library normalization was performed using the calcNormFactors function.

788 To account for tumor grade, a similar analysis was performed with tumor grade as a blocking
789 factor in the model design. Due to the inability of the exactTest to handle complex experimental
790 designs, a quasi-likelihood negative binomial generalized log-linear model (glmQLFTest) was
used to determine differentially expressed genes for this analysis⁸³.

792 Genes with log counts per million < 1.5 in the higher-expressing sample group were excluded
from further analysis (Supplementary Material, **Table S4 – complete pseudobulk analysis
results for T and NK cells, myeloid cells, and epithelial cells**).

794

Pseudotime analysis of scRNA-seq data

796 Linear pseudotime ordering was performed for a subset of six T cell clusters (T-naive, T-
797 cytotoxic-1 to -4, and T-CD8-exhausted) using the Bayesian latent variable statistical
798 framework Oujia⁴⁶ with 6000 iterations. To speed up calculations, only a random subsample
of 800 cells per patient from this T cell subset was used as input. A set of 23 putative marker
800 genes was used for pseudotime learning (Supplementary Material, **Table S5 – gene lists and
gene signatures**) and individual cells were ranked by assigned pseudotime values for further
802 analysis. Mean pseudotimes for patient samples and clusters were calculated as the average
pseudotime rank for all T cells of the respective sample/cluster that were included in Oujia
804 analysis.

806 To study the origin of migDCs, pseudotime analysis without predefined topology was
performed on a subset of three myeloid clusters (cDC1, cDC2, and migDC) using Slingshot
808 (v1.7.3)⁸⁴ and Monocle (v2.12)⁸⁵. Slingshot pseudotime values were extracted for the cDC2-
migDC transition (excluding cDC1), cells were ranked by pseudotime and gene expression
810 along pseudotime rank was plotted using the rolling average over 11 cells (selected as a good
granularity for visualizing the major trends in the plot, Fig. 4H). Mean DC pseudotime per
812 patient sample was calculated as the average pseudotime rank of all cDC2 and migDC cells
in the sample (Fig. S8G).

814

Identification of myeloid cell gene signatures

816 In order to interpret gene expression patterns observed across myeloid cells in the context of
defined functional states, we compiled four distinct gene signatures. To assemble the T cell-
818 attractive and the T cell-suppressive myeloid cell gene signatures we performed a broad
literature survey and manually extracted genes reportedly involved in chemoattraction or
820 myeloid-mediated suppression of T cells (Supplementary Material, **Table S5 – gene lists and
gene signatures**). Gene lists for the M1 and M2 signatures were adopted from Azizi et al.²⁷.
822 Prior to summing up signature gene counts to calculate a score for each signature in each
cell, individual gene counts were normalized by the total cellular gene count and log-
824 transformed to reduce the relative dominance of highly expressed genes. Given that we only
observed positive signature score correlations in our analysis, we also assembled a random
826 control gene signature and found no correlation with either the attractive or the suppressive T

828 cell signature indicating that there were no experimental or computational biases (data not
shown).

830

Combined ligand-receptor analysis using scRNA-seq data

832 *SingleCellSignalR*

To assess cell-to-cell communication, we first used the SingleCellSignalR package⁵⁸. For
834 SingleCellSignalR analysis of main cell type interactions, we subsampled 10,000 cells for each
of the cell types and calculated interaction scores for all ligand-receptor pairs over all cell type
836 pairs. Autocrine and paracrine interaction scores were calculated separately and then merged
into a single matrix. An empirically selected ligand-receptor (LR) score threshold of 0.4 was
838 used to define and quantify “true” interaction pairs for each cell type pair as recommended⁶⁰
(Fig. 5A, Fig. S9A). In order to extract the most relevant hits, we wanted to identify high-
840 scoring, cell type pair-specific interactions. To this end, the 100 highest-scoring ligand-
receptor interactions for each cell type were extracted, followed by identification of the five
842 ligand-receptor pairs with the highest coefficient of variation between all cell type pairs (i.e.,
the five most specific interactions for the respective cell type pair) (Supplementary Material,
844 **Table S6 – SingleCellSignalR output**). Of these, pairs were manually selected for plotting
based on solidity of the literature evidence and biological interpretability of the interaction (Fig.
846 5B). SingleCellSignalR analysis of the T and NK cell metacluster and myeloid cell metacluster
interactions was performed in the same way and with the same cutoffs (Fig. 5C). In Fig. S9C,
848 all interactions involving LC, pDC, or T-mixed as well as myeloid-myeloid and T and NK-T and
NK interactions were excluded for clarity.

850 To compare ligand-receptor interactions between IE1- and IE2-classified tumors,
SingleCellSignalR analysis for epithelial cell, myeloid cell, and T and NK cell interactions was
852 performed for each patient sample separately. The difference between LR scores of IE1 and
IE2 samples were assessed using Wilcoxon rank-sum testing for each ligand-receptor pair in
854 each cell type pair. Among all interactions with $p < 0.05$ (not corrected for multiple hypothesis
testing) and a mean LR score > 0.4 , the biologically most relevant and literature-backed
856 interactions were chosen for plotting (Fig. 5B). Complete results can be found in the
Supplementary Material (**Table S6 – SingleCellSignalR output**).

858 *CellPhoneDB*

CellPhoneDB, another algorithm for ligand-receptor analysis⁸⁶, was used to assess the
860 consistency of our SingleCellSignalR results. One major difference between the two
algorithms is that CellPhoneDB defines the significance of ligand-receptor interactions based
862 on random permutation of cluster labels, leading to large p values for interactions that are
present in many different cluster pairs. To analyze and quantify the interactions in the main
864 cell types, we subsampled 3,000 cells per cell type and ran CellPhoneDB in Python with 1,000
iterations (**Supplementary Material, Table S7 – CellPhoneDB output**). As for
866 SingleCellSignalR analysis, we compared ligand-receptor interactions between IE1 and IE2
tumors by running CellPhoneDB on each patient sample separately and testing for enrichment

868 of ligand-receptor pairs in either of the two IEs. The results were in good agreement with the
SingleCellSignalR findings (Fig. S9D).

870 *NicheNet*

To predict which myeloid-derived ligands are the most closely linked to T cell exhaustion in
872 our dataset we used NicheNet, a method that combines single cell expression data with prior
knowledge on signaling networks and predicts which sender cell ligands are most likely to
874 have affected the expression of a set of known target genes in the receiver cells⁸⁷. For this
analysis, we defined all myeloid cells as sender cells and all CD8+ and naïve T cell clusters
876 as receiver cells. The target gene set included all genes that were specifically upregulated in
the T-CD8-exhausted cluster as determined by differential expression analysis. NicheNet
878 quantifies ligand activity by determining the Pearson correlation coefficient between a ligand's
a priori target predictions and the observed transcriptional response, with higher ranking
880 ligands having a better ability to predict the target gene set compared to the background of
expressed genes.

882

Classification of CD8+ T cell infiltration status

884 The CD8+ T cell infiltration status was independently assessed by a clinical pathologist based
on the spatial distribution of CD8+ T cells on whole-slide H&E and IHC stains as described
886 previously⁴³. In brief, tumors were classified as (i) immune desert if there were no (or very few)
CD8+ T cells in the intratumoral and stromal compartment or at the tumor margin, as (ii)
888 immune-excluded if CD8+ T cells were only found at the tumor margin or in the stromal
compartment but not infiltrating the tumor mass, or as (iii) inflamed if CD8+ T cells had
890 infiltrated the tumor mass and were found in direct contact with tumor cells. Desert and
immune-excluded phenotypes are generally classified as “immune-cold”, while inflamed
892 phenotypes are classified as “immune-hot”.

894 **IMC panels**

For spatial analysis of the breast immune environment, we designed and validated two IMC
896 panels that included antibodies against canonical cell type markers and known
immunoregulatory targets with a focus on markers differentially expressed in IE1 versus IE2
898 in our scRNA-seq pseudobulk analysis. The Protein Panel was an all-antibody panel, and the
RNA Panel was an RNAscope panel that included 10 cytokine/chemokine-targeting mRNA
900 probes, one negative control mRNA probe (*DapB*), and one mRNA probe targeting *MS4A1*
(the gene encoding CD20). More detailed information can be found in **Supplementary Table**
902 **S8**.

904

IMC sample preparation and immunofluorescence whole-slide scans

906 Twelve samples were analyzed by IMC. For each, two consecutive 4- μ m thick sections (for
908 staining with two different panels) were cut from the respective FFPE tissue block and
processed on slides with a combination of immunofluorescence and IMC staining. Slides
910 intended for staining with the Protein Panel were deparaffinized in HistoClear (Biosystems)
three times (10 min per incubation) before being rehydrated in a graded alcohol series
912 (ethanol:deionized water 100:0, 90:10, 80:20, 70:30, 50:50, 0:100; 5-10 min each). Antigen
retrieval was performed in Tris-EDTA buffer (pH 9) at 95 °C for 30 min in a NxGen decloaking
914 chamber (Biocare Medical). After cool-down, slides were blocked with 3% BSA in TBS (20
mM Tris (pH 7.6), 150 mM NaCl) for 1 h. Samples were first stained with rabbit anti-CD3 and
916 mouse anti-CD20 overnight at 4 °C. Primary antibodies used at this stage were metal-tagged.
Slides were washed three time (5 min per wash) in TBS before staining with fluorescently
918 labeled secondary antibodies (anti-rabbit-Alexa750 and anti-mouse-Alexa555) for 1 h at room
temperature. Slides were then stained with DAPI (1:500 in PBS), washed again three times (5
920 min per wash) in TBS and stained with the remaining metal-tagged antibodies of the Protein
Panel overnight at 4 °C. The next day, slides were washed three times (5 min per wash) in
922 TBS and stained with a final concentration of 0.5 μ M Cell ID Intercalator-Ir (Fluidigm) for 5 min
at room temperature. Slides were washed again in TBS (three times, 5 min per wash), dipped
in deionized water, and dried with pressured air.

924 Slides to be stained with the RNA Panel were processed as previously described^{24,88}. Antigen
retrieval and RNA staining were performed with an RNAscope Fluorescence Multiplex
926 Reagent Kit (Advanced Cell Diagnostics) according to manufacturer's instructions. Detection
oligonucleotides were metal-conjugated as described²⁴ and used at a final concentration of 20
928 nM. After the last wash step of the RNAscope protocol, slides were washed for 3 min in TBS
and stained with metal-tagged rabbit anti-CD68, mouse anti-panCK, and mouse anti-E-
930 cadherin overnight at 4 °C. Slides were then processed as described above with fluorescently
labeled secondary antibody staining followed by DAPI staining, staining with the RNA Panel,
932 and iridium staining before the final washes and slide drying. Immediately after drying, an Axio
Scan Z.1 (Zeiss) was used for multi-channel fluorescence whole-slide scanning of all sections.

934

IMC region selection and data acquisition

936 For IMC, four to six representative ROIs were selected for each slide based on the
immunofluorescence pre-scan. Immature and mature TLS regions were defined on the
938 immunofluorescence pre-scans as sites of B cell accumulation without a clear center or sites
with dense round B cell accumulation, respectively³². If present, one to five of these regions
940 were additionally imaged per sample. All ROIs were 1 mm x 1 mm and were manually aligned
for each pair of consecutive tissue cuts to ensure the best possible overlap between images
942 from the two different panels. In total, 154 multiplexed images were acquired at 400 Hz using
a Hyperion Imaging System (Fluidigm), and the raw data were pre-processed using
944 commercial software (Fluidigm) (Supplementary Material, **Table S9 – ROI metadata**).

946 IMC data processing

948 Images files were converted from the commercial format to OME-TIFF, and single cells were
949 segmented using a combination of ilastik⁸⁹ v.1.3.3 and CellProfiler⁹⁰ v.3.1.9 as described in
the workflow available at <https://github.com/BodenmillerGroup/ImcSegmentationPipeline>⁹¹.
950 Signal spillover between channels was compensated on the single-cell level using the R
package CATALYST⁹² (v1.8.7), and high-dimensional averaged marker expression as well as
952 spatial features were extracted for each cell using CellProfiler⁹¹. Cells on the edges of each
image were discarded. Single-cell objects extracted from tissue sections represent small
954 tissue slices that potentially contain overlapping cell fragments despite high-quality
segmentation. Especially in densely packed regions, the extracted single-cell marker
956 expression may thus include some information originating from neighboring cells. To extract
spatial cellular relationships, the circumference of each cell was expanded by 8 pixels (8 μm)
958 and overlapping cells were defined as neighbors.

960 **IMC analysis workflow and clustering**

IMC downstream analysis was conducted in R v.4.0.2. For each of the two panels, the single-
962 cell expression matrix was converted into a SingleCellExperiment object⁹³ with the
corresponding metadata attached, and a filter was applied to exclude cells with an area < 8
964 pixels or > 600 pixels. We used different data transformations for different downstream
analysis steps as indicated in the figures: Single-cell marker expression was either (i) arcsinh-
966 transformed, scaled, and centered or (ii) 01-normalized for each marker using the 99th
percentile normalization to account for outliers. A multi-step graph-based clustering approach
968 based on the 01-normalized data was used to identify single-cell phenotypes. For each
clustering step, a shared nearest neighbor graph was built using the scran R package
970 (v.1.16.0)⁹⁴ followed by Louvain community detection as implemented in igraph (v.1.2.5)⁹⁵. For
each of the panels, the first clustering step was performed with a selected set of cell type
972 markers (**see Suppl. Table S8**), and each cluster was annotated as epithelial or non-epithelial
based primarily on expression of panCK and E-Cadherin. Non-epithelial cell clusters were
974 pooled and subjected to a second clustering step with similar markers (excluding epithelial
markers; see Fig. S2F and Fig. S3B for markers used) to identify immune and stromal cell
976 types in higher granularity. Annotation of stromal and immune cell subtypes was based on
canonical marker expression. For the Protein Panel data only, T cell clusters were subsetted
978 and subjected to a third clustering step with T cell-specific markers such as PD-1 and ICOS
(see Fig. S5B for markers used). To identify Ki-67⁺ T cells, an empirical cutoff of 0.7 was
980 chosen on Ki-67 arcsinh-transformed counts. In addition, epithelial cells from the Protein Panel
that were proliferating, hypoxic, or apoptotic were identified using empirically defined cut-offs
982 for Ki-67 expression, Carbonic Anhydrase XI expression, and Cleaved Caspase/Cleaved
PARP expression, respectively. The percentage of Ki-67⁺ epithelial cells in each patient
984 sample as determined by IMC was strongly correlated to the percentage determined by
immunohistochemistry in standard clinical diagnostics (Spearman's $\rho = 0.77$, $p = 0.0037$),
986 confirming sensible cut-off selection. We used the scater implementation⁹⁶ of the
dimensionality reduction algorithm UMAP for two-dimensional visualization of high-
988 dimensional single-cell data. For the full datasets, the algorithm was run on a random
subsample of 10,000 cells per patient sample to avoid overcrowding of data points. For data
990 subsets, the algorithm was run on all cells.

992 **Cytokine expression status**

994 In the RNA Panel dataset, a binary cytokine expression status for each of the cytokines
996 measured on mRNA level was assigned to every cell as previously described⁸⁸. In brief, the
998 difference between the respective cytokine signal and the signal of the negative control mRNA
probe (*DapB*) was determined for each cell, p values were calculated from the distribution of
differences, and a threshold of $p < 0.01$ after Benjamini-Hochberg correction was applied to
define cytokine-expressing cells.

1000 **Cytokine patches and milieus**

1002 Cytokine patches and cytokine milieus were defined as previously described⁸⁸. In short,
1004 cytokine patches were defined as a minimum of three neighboring cells all expressing at least
1006 one cytokine (general cytokine patch) or all expressing the same cytokine (cytokine-specific
1008 patch). For this analysis, the maximum distance for two cells to be considered neighbors was
25 μm . To define cytokine milieus, the cytokine patch borders were extended by 30 μm and
all cells within this radius were included in the respective cytokine milieu. For each individual
image, enrichment or depletion of a cell type X in a milieu type Y was calculated using a
Fisher's exact test. The threshold for significance was $p < 0.01$ and only images that contained
both X and Y were used to quantify the percentage of images with significant enrichment or
depletion of X in Y.

1012 **Functional gene signature validation by IMC**

1014 To validate the T cell-attractive myeloid cell gene signatures, we used the RNA Panel dataset
1016 and split myeloid cells into two groups based on whether or not they expressed at least one
of the measured T cell-attracting chemokines (*CXCL9*, *CXCL10*, *CCL2*, *CCL17*, *CCL4*, *CCL5*).
1018 Subsequently, the distance to the closest T cell was compared for chemokine-expressing and
non-expressing myeloid cells. Of the genes used to construct the T cell-suppressive myeloid
cell gene signature, only antibodies targeting corresponding proteins IDO1 and PD-L1 were
1020 included in our IMC panels. For validation of this signature, we thus split myeloid cells of the
protein panel IMC dataset into a "suppressive" group (high expression of PD-L1 and/or IDO1)
1022 and a "non-suppressive" group. For every myeloid cell, we then identified the 10 closest T
cells (excluding T_{regs}), calculated the proportion of PD-1^{high} T cells among these, and compared
this proportion for suppressive versus non-suppressive myeloid cells.

1024

Pairwise neighborhood analysis

1026 The Protein Panel dataset was used for neighborhood analysis because it allowed a more
1028 fine-grained annotation of cellular subtypes than did the RNA Panel. To identify significantly
enriched or depleted pairwise neighbor interactions between cell types, a two-sided

1030 permutation-test-based analysis with 1,000 permutations per image was performed as
described previously⁶⁰. The threshold for significant interactions was $p < 0.01$.

1032 **Image visualization**

1034 All pixel and single-cell level images shown in the figures were generated using the
cytomapper R package (v.1.0.0)⁹⁷.

1036 **Whole-slide immunofluorescence screen for TLS classification**

1038 To screen for mature TLS and immature TLS, we used FFPE slides from 13 additional patients
included in the Wagner et al. cohort²⁹ that were classified as either IE1 or IE2 (corresponding
1040 to TIG2 and TIG3 in Wagner et al.). Slide pre-processing and antigen retrieval were performed
as described above for slides stained with the Protein Panel. After blocking with 3% BSA in
1042 TBS, slides were stained with rat anti-CD3, rabbit anti-CD68, and mouse anti-CD20 overnight
at 4 °C (**Table S8**). The next day, slides were washed in TBS (three times, 5 min per wash)
1044 and stained with fluorescently labeled secondary antibodies (**Table S8**) for 1 h at room
temperature. Slides were washed again in TBS (three times, 5 min per wash), and a coverslip
1046 was mounted using a polyvinyl alcohol mounting medium. Fluorescent whole-slide images
were acquired with an Axio Scan Z.1. Mature and immature TLS sites were defined as above
1048 (see IMC region selection and data acquisition section) and annotated in an IE-blinded
manner.

1050 **Data and code availability**

1052 All data and code will be made available upon publication. RNA-seq data have been deposited
in the ArrayExpress database at EMBL-EBI (<https://www.ebi.ac.uk/arrayexpress>) under
accession number E-MTAB-10607. Imaging Mass Cytometry data have been deposited on
1054 Zenodo (DOI: 10.5281/zenodo.4911135) and will be made publicly accessible upon
publication.

1056 **REFERENCES**

- 1058 1. Sosman, J. A. *et al.* Improved Survival with Ipilimumab in Patients with Metastatic Melanoma. *N. Engl. J. Med.* **363**, 711–723 (2010).
- 1060 2. Robert, C. *et al.* Durable Complete Response After Discontinuation of Pembrolizumab in Patients With Metastatic Melanoma. *J. Clin. Oncol.* **36**, (2018).
- 1062 3. Berghmans, T., Dingemans, A., Hendriks, L. E. L. & Cadranel, J. Immunotherapy for nonsmall cell lung cancer : a new therapeutic algorithm. *Eur. Respir. J.* **55**, (2020).
- 1064 4. Wang, J. *et al.* Role of immune checkpoint inhibitor-based therapies for metastatic renal cell carcinoma in the first-line setting : A Bayesian network analysis. *EBioMedicine* **47**, 78–88 (2019).
- 1066 5. Vonderheide, R. H., Domchek, S. M. & Clark, A. S. Immunotherapy for breast cancer: What are we missing? *Clin. Cancer Res.* **23**, 2640–2646 (2017).
- 1068 6. Ali, H. R., Chlon, L., Pharoah, P. D. P., Markowitz, F. & Caldas, C. Patterns of Immune Infiltration in Breast Cancer and Their Clinical Implications : A Gene-Expression-Based Retrospective Study. *PLoS Med.* **13(12)**, 1–24 (2016).
- 1070 7. Park, Y. H. *et al.* Chemotherapy induces dynamic immune responses in breast cancers that impact treatment outcome. *Nat. Commun.* **11**, 1–14 (2020).
- 1072 8. Denkert, C. *et al.* Tumour-infiltrating lymphocytes and prognosis in different subtypes of breast cancer: a pooled analysis of 3771 patients treated with neoadjuvant therapy. *Lancet Oncol.* **19**, 40–50 (2018).
- 1074 9. Kwapisz, D. Pembrolizumab and atezolizumab in triple-negative breast cancer. *Cancer Immunol. Immunother.* **1**, (2020).
- 1076 10. Raskov, H. Cytotoxic CD8 + T cells in cancer and cancer immunotherapy. *Br. J. Cancer* (2020) doi:10.1038/s41416-020-01048-4.
- 1078 11. Matsushita, H., Hosoi, A., Ueha, S., Abe, J. & Fujieda, N. Cytotoxic T Lymphocytes Block Tumor Growth Both by Lytic Activity and IFN γ -Dependent Cell-Cycle Arrest. *Cancer Immunol. Res.* **3**, 26–37 (2015).
- 1080 12. Thommen, D. S. & Schumacher, T. N. T Cell Dysfunction in Cancer. *Cancer Cell* **33**, 547–562 (2018).
- 1082 13. Li, H. *et al.* Dysfunctional CD8 T Cells Form a Proliferative, Dynamically Regulated Compartment within Human Melanoma. *Cell* **176**, 1–15 (2018).
- 1084 14. Zhang, L. *et al.* Lineage tracking reveals dynamic relationships of T cells in colorectal cancer. *Nature* **564**, (2018).
- 1086 15. Bassez, A. *et al.* A single-cell map of intratumoral changes during anti-PD1 treatment of patients with breast cancer. *Nature Medicine* (Springer US, 2021). doi:10.1038/s41591-021-01323-8.
- 1088 16. Egelston, C. A. *et al.* Human breast tumor-infiltrating CD8+ T cells retain polyfunctionality despite PD-1 expression. *Nat. Commun.* **9**, 1–11 (2018).

- 1094 17. DeNardo, D. G. & Ruffell, B. Macrophages as regulators of tumour immunity and immunotherapy. *Nat. Rev. Immunol.* **19**, 369–382 (2019).
- 1096 18. Wculek, S. K. *et al.* Dendritic cells in cancer immunology and immunotherapy. *Nat. Rev. Immunol.* **20**, 7–24 (2020).
- 1098 19. Murdoch, C., Muthana, M., Coffelt, S. B. & Lewis, C. E. The role of myeloid cells in the promotion of tumour angiogenesis. *Nat. Rev. Cancer* **8**, (2008).
- 1100 20. Chen, W. *et al.* A multicenter study benchmarking single-cell samples. *Nat. Biotechnol.* doi:10.1038/s41587-020-00748-9.
- 1102 21. Ijsselsteijn, M. E., van der Breggen, R., Sarasqueta, A. F., Koning, F. & de Miranda, N. F. C. C. A 40-marker panel for high dimensional characterization of cancer immune microenvironments by imaging mass cytometry. *Front. Immunol.* **10**, 1–8 (2019).
- 1104
- 1106 22. Chevrier, S. *et al.* An Immune Atlas of Clear Cell Renal Cell Carcinoma. *Cell* **169**, 736–749 (2017).
- 1108 23. Giesen, C. *et al.* Highly multiplexed imaging of tumor tissues with subcellular resolution by mass cytometry. *Nat. Methods* **11**, 417–422 (2014).
- 1110 24. Schulz, D. *et al.* Simultaneous Multiplexed Imaging of mRNA and Proteins with Subcellular Resolution in Breast Cancer Tissue Samples by Mass Cytometry. *Cell Syst.* **6**, (2017).
- 1112 25. Jackson, H. W. *et al.* The single-cell pathology landscape of breast cancer. *Nature* **578**, 615–620 (2020).
- 1114 26. Keren, L. *et al.* A Structured Tumor-Immune Microenvironment in Triple Negative Breast Cancer Revealed by Multiplexed Ion Beam imaging. *Cell* **174**, 1373–1387 (2018).
- 1116
- 1118 27. Azizi, E. *et al.* Single-Cell Map of Diverse Immune Phenotypes in the Breast Tumor Microenvironment. *Cell* **174**, 1–16 (2018).
- 1120 28. Yuan, X., Wang, J., Huang, Y., Shanguan, D. & Zhang, P. Single-Cell Profiling to Explore Immunological Heterogeneity of Tumor Microenvironment in Breast Cancer. *Front. Immunol.* **12**, 1–7 (2021).
- 1122 29. Wagner, J. *et al.* A Single-Cell Atlas of the Tumor and Immune Ecosystem of Human Breast Cancer. *Cell* **177**, 1–16 (2019).
- 1124 30. Deutsch, A., Feng, D., Pessin, J. E. & Shinoda, K. The Impact of Single-Cell Genomics on Adipose Tissue Research. *Int. J. Mol. Sci.* **21**, (2020).
- 1126 31. Graham-Pole, J., Davie, M. & Willoughby, M. L. N. Cryopreservation of human granulocytes in liquid nitrogen. *J. Clin. Pathol.* **30**, 758–762 (1977).
- 1128 32. Li, Q. *et al.* Prognostic value of tertiary lymphoid structure and tumour infiltrating lymphocytes in oral squamous cell carcinoma. *Int. J. Oral Sci.* **12**, 1–8 (2020).
- 1130 33. Judge, S. J., Murphy, W. J. & Canter, R. J. Characterizing the Dysfunctional NK Cell: Assessing the Clinical Relevance of Exhaustion, Anergy, and Senescence. *Front. Cell. Infect. Microbiol.* **10**, (2020).
- 1132

- 1134 34. Nayar, R. *et al.* TCR signaling via Tec kinase ITK and interferon regulatory factor 4 (IRF4) regulates CD8+ T-cell differentiation. *Proc. Natl. Acad. Sci. U. S. A.* **109**, (2012).
- 1136 35. Kurachi, M. *et al.* The transcription factor BATF operates as an essential
1138 differentiation checkpoint in early effector CD8 + T cells. *Nat. Immunol.* **15**, 373–383 (2014).
- 1140 36. Scott, A. C. *et al.* TOX is a critical regulator of tumour-specific T cell differentiation. *Nature* **571**, 270–274 (2019).
- 1142 37. Sade-Feldman, M. *et al.* Defining T Cell States Associated with Response to Checkpoint Immunotherapy in Melanoma. *Cell* **175**, 998–1013 (2018).
- 1144 38. Schrum, A. G., Turka, L. A. & Palmer, E. Surface T-cell antigen receptor expression and availability for long-term antigenic signaling. *Immunol. Rev.* **196**, 7–24 (2003).
- 1146 39. Paillard, F., Sterkers, G., Bismuth, G., Gomard, E. & Vaquero, C. Lymphokine mRNA and T cell multireceptor mRNA of the Ig super gene family are reciprocally modulated during human T cell activation. *Eur. J. Immunol.* **18**, 1643–1646 (1988).
- 1148 40. Savas, P. *et al.* Single-cell profiling of breast cancer T cells reveals a tissue-resident memory subset associated with improved prognosis. *Nat. Med.* **24**, 986–993 (2018).
- 1150 41. van der Leun, A. M., Thommen, D. S. & Schumacher, T. N. CD8+ T cell states in
1152 human cancer: insights from single-cell analysis. *Nat. Rev. Cancer* **20**, 218–232 (2020).
- 1154 42. Duhon, T. *et al.* Co-expression of CD39 and CD103 identifies tumor-reactive CD8 T cells in human solid tumors. *Nat. Commun.* **9**, (2018).
- 1156 43. Sobottka, B., Moch, H. & Varga, Z. Differential PD-1 / LAG-3 expression and immune phenotypes in metastatic sites of breast cancer. *Breast Cancer Res.* **23**, 1–11 (2021).
- 1158 44. Hornburg, M. *et al.* Single-cell dissection of cellular components and interactions shaping the tumor immune phenotypes in ovarian cancer. *Cancer Cell* 1–17 (2021) doi:10.1016/j.ccell.2021.04.004.
- 1160 45. Gu-Trantien, C. & Willard-Gallo, K. Tumor-infiltrating follicular helper T cells: The new kids on the block. *Oncoimmunology* **2**, 8–10 (2013).
- 1162 46. Campbell, K. R. & Yau, C. A descriptive marker gene approach to single-cell pseudotime inference. *Bioinformatics* **35**, 28–35 (2019).
- 1164 47. Terabe, M. & Berzofsky, J. A. Tissue-specific roles of NKT cells in tumor immunity. *Front. Immunol.* **9**, 1–11 (2018).
- 1166 48. Boulakirba, S. *et al.* IL-34 and CSF-1 display an equivalent macrophage differentiation ability but a different polarization potential. *Sci. Rep.* **8**, 1–11 (2018).
- 1168 49. Chen, J. *et al.* CCL18 from Tumor-Associated Macrophages Promotes Breast Cancer Metastasis via PITPNM3. *Cancer Cell* **19**, 541–555 (2011).
- 1170 50. Cui, W. *et al.* HBXIP upregulates CD46, CD55 and CD59 through ERK1/2/NF- κ B signaling to protect breast cancer cells from complement attack. *FEBS Lett.* **586**, 766–

- 1172 771 (2012).
- 1174 51. Merdad, A., Karim, S., Schulten, H. & Dallol, A. Expression of Matrix
Metalloproteinases (MMPs) in Primary Human Breast Cancer : MMP-9 as a Potential
1176 Biomarker for Cancer Invasion and Metastasis. *Anticancer Res.* **34**, 1355–1366
(2014).
- 1178 52. Hubert, M. *et al.* IFN-III is selectively produced by cDC1 and predicts good clinical
outcome in breast cancer. *Sci. Immunol.* **5**, eaav3942 (2020).
- 1180 53. Park, J.-E. *et al.* A cell atlas of human thymic development defines T cell repertoire
formation. *Science* **367**, (2020).
- 1182 54. Zhang, Q. *et al.* Landscape and Dynamics of Single Immune Cells in Hepatocellular
Carcinoma. *Cell* **179**, 829-845.e20 (2019).
- 1184 55. Maier, B. *et al.* A conserved dendritic-cell regulatory program limits antitumour
immunity. *Nature* **580**, (2020).
- 1186 56. Cheng, S. *et al.* A pan-cancer single-cell transcriptional atlas of tumor infiltrating
myeloid cells. *Cell* **184**, 792-809.e23 (2021).
- 1188 57. Qian, J. *et al.* A pan-cancer blueprint of the heterogeneous tumor microenvironment
revealed by single-cell profiling. *Cell Res.* **30**, 745–762 (2020).
- 1190 58. Cabello-Aguilar, S. *et al.* SingleCellSignalR: inference of intercellular networks from
single-cell transcriptomics. *Nucleic Acids Res.* **48**, e55 (2020).
- 1192 59. Karsunky, H., Merad, M., Cozzio, A., Weissman, I. L. & Manz, M. G. Flt3 ligand
regulates dendritic cell development from Flt3+ lymphoid and myeloid-committed
progenitors to Flt3+ dendritic cells in vivo. *J. Exp. Med.* **198**, 305–313 (2003).
- 1194 60. Schapiro, D. *et al.* histoCAT: analysis of cell phenotypes and interactions in multiplex
image cytometry data. *Nat. Methods* **14**, (2017).
- 1196 61. Colbeck, E. J., Ager, A., Gallimore, A. & Jones, G. W. Tertiary lymphoid structures in
1198 cancer: Drivers of antitumor immunity, immunosuppression, or Bystander Sentinels in
disease? *Front. Immunol.* **8**, 1–18 (2017).
- 1200 62. Workel, H. H. *et al.* A Transcriptionally Distinct CXCL13 + CD103 + CD8 + T-cell
Population Is Associated with B-cell Recruitment and Neoantigen Load in Human
Cancer. *Cancer Immunol. Res.* **7**, 784–796 (2019).
- 1202 63. Valla, M. *et al.* Molecular subtypes of breast cancer: Long-term incidence trends and
prognostic differences. *Cancer Epidemiol. Biomarkers Prev.* **25**, 1625–1634 (2016).
- 1204 64. Caroline, J., Stotz, L. & Canguel, A. Clinical Data on Immunotherapy in Breast
Cancer. *Breast Care* **15**, 450–469 (2020).
- 1206 65. Aptsiauri, N., Ruiz-Cabello, F. & Garrido, F. The transition from HLA-I positive to HLA-
1208 I negative primary tumors: the road to escape from T-cell responses. *Curr. Opin.
Immunol.* **51**, 123–132 (2018).
- 1210 66. Zhang, X. *et al.* Breast cancer neoantigens can induce CD8+ T-cell responses and
antitumor immunity. *Cancer Immunol. Res.* **5**, 516–523 (2017).

- 1212 67. Ghorani, E. *et al.* The T cell differentiation landscape is shaped by tumour mutations in lung cancer. *Nat. Cancer* **1**, 546–561 (2020).
- 1214 68. Gonzalez-Avila, G. *et al.* Matrix metalloproteinases participation in the metastatic process and their diagnostic and therapeutic applications in cancer. *Crit. Rev. Oncol. / Hematol.* **137**, 57–83 (2019).
- 1216 69. Gu-Trantien, C. *et al.* CD4 + follicular helper T cell infiltration predicts breast cancer survival. *J. Clin. Investig. invest.* **123**, 2873–2892 (2013).
- 1218 70. Martinet, L. *et al.* Human solid tumors contain high endothelial venules: Association with T- and B-lymphocyte infiltration and favorable prognosis in breast cancer. *Cancer Res.* **71**, 5678–5687 (2011).
- 1220
- 1222 71. Figenschau, S. L., Fismen, S., Fenton, K. A., Fenton, C. & Mortensen, E. S. Tertiary lymphoid structures are associated with higher tumor grade in primary operable breast cancer patients. *BMC Cancer* **15**, 1–11 (2015).
- 1224 72. Lee, H. J. *et al.* Tertiary lymphoid structures : Prognostic significance and relationship with tumour-infiltrating lymphocytes in triple-negative breast cancer. *J. Clin. Pathol.* **69**, 422–430 (2016).
- 1226
- 1228 73. Lee, M. *et al.* Presence of tertiary lymphoid structures determines the level of tumor-infiltrating lymphocytes in primary breast cancer and metastasis. *Mod. Pathol.* **32**, 70–80 (2019).
- 1230 74. Muenst, S. *et al.* The presence of programmed death 1 (PD-1)-positive tumor-infiltrating lymphocytes is associated with poor prognosis in human breast cancer. *Breast Cancer Res Treat* **139**, (2013).
- 1232
- 1234 75. Zhang, Y. *et al.* Single-cell analyses reveal key immune cell subsets associated with response to PD-L1 blockade in triple-negative breast cancer. *Cancer Cell* 1–16 (2021) doi:10.1016/j.ccell.2021.09.010.
- 1236 76. Adams, S. *et al.* Current Landscape of Immunotherapy in Breast Cancer: A Review. *JAMA Oncol.* **5**, 1205–1214 (2019).
- 1238 77. Stuart, T. *et al.* Comprehensive Integration of Single-Cell Data. *Cell* **177**, 1888-1902.e21 (2019).
- 1240 78. McGinnis, C. S., Murrow, L. M. & Gartner, Z. J. DoubletFinder: Doublet Detection in Single-Cell RNA Sequencing Data Using Artificial Nearest Neighbors. *Cell Syst.* **8**, 329-337.e4 (2019).
- 1242
- 1244 79. Hafemeister, C. & Satija, R. Normalization and variance stabilization of single-cell RNA-seq data using regularized negative binomial regression. *Genome Biol.* **20**, 576827 (2019).
- 1246 80. McInnes, L., Healy, J., Saul, N. & Großberger, L. UMAP: Uniform Manifold Approximation and Projection. *J. Open Source Softw.* **3**, 861 (2018).
- 1248 81. Finak, G. *et al.* MAST: A flexible statistical framework for assessing transcriptional changes and characterizing heterogeneity in single-cell RNA sequencing data. *Genome Biol.* **16**, 1–13 (2015).
- 1250

- 1252 82. Zappia, L. & Oshlack, A. Clustering trees: a visualization for evaluating clusterings at multiple resolutions. *Gigascience* **7**, 1–9 (2018).
- 1254 83. Robinson, M. D., McCarthy, D. J. & Smyth, G. K. edgeR: A Bioconductor package for differential expression analysis of digital gene expression data. *Bioinformatics* **26**, 139–140 (2009).
- 1256 84. Street, K. *et al.* Slingshot: cell lineage and pseudotime inference for single-cell transcriptomics. *BMC Genomics* **19**, 1–16 (2018).
- 1258 85. Qiu, X. *et al.* Single-cell mRNA quantification and differential analysis with Census. *Nat. Methods* **14**, 309–315 (2017).
- 1260 86. Efremova, M., Vento-Tormo, M., Teichmann, S. A. & Vento-Tormo, R. CellPhoneDB: inferring cell–cell communication from combined expression of multi-subunit ligand–receptor complexes. *Nat. Protoc.* **15**, 1484–1506 (2020).
- 1262
- 1264 87. Browaeys, R., Saelens, W. & Saeys, Y. NicheNet : modeling intercellular communication by linking ligands to target genes. *Nat. Methods* doi:10.1038/s41592-019-0667-5.
- 1266 88. Hoch, T. *et al.* Multiplexed Imaging Mass Cytometry of Chemokine Milieus in Metastatic Melanoma Characterizes Features of Response to Immunotherapy. *bioRxiv* 2021.07.29.454093 (2021).
- 1268
- 1270 89. Berg, S. *et al.* Ilastik: Interactive Machine Learning for (Bio)Image Analysis. *Nat. Methods* **16**, 1226–1232 (2019).
- 1272 90. McQuin, C. *et al.* CellProfiler 3.0: Next-generation image processing for biology. *PLoS Biol.* **16**, 1–17 (2018).
- 1274 91. Zanutelli, V., Damond, N. & Strotton, M. ImcSegmentationPipeline: A pixel classification based multiplexed image segmentation pipeline | Zenodo. <https://zenodo.org/record/3841961>.
- 1276 92. Chevrier, S. *et al.* Compensation of Signal Spillover in Suspension and Imaging Mass Cytometry. *Cell Syst.* **6**, 612-620.e5 (2018).
- 1278 93. Amezcua, R. A. *et al.* Orchestrating single-cell analysis with Bioconductor. *Nat. Methods* **17**, 137–145 (2020).
- 1280 94. Lun, A. T. L., McCarthy, D. J., Marioni, J. C. & McDavid, A. A step-by-step workflow for low-level analysis of single-cell RNA-seq data with Bioconductor. *F1000 Res.* **5**, (2016).
- 1282
- 1284 95. Csardi, G. & Nepusz, T. The igraph software package for complex network research. *InterJournal* 1695 (2006).
- 1286 96. McCarthy, D. J., Campbell, K. R., Lun, A. T. L. & Wills, Q. F. Scater: pre-processing, quality control, normalization and visualization of single-cell RNA-seq data in R. *Bioinformatics* **33**, 1179–1186 (2017).
- 1288 97. Eling, N., Damond, N., Hoch, T. & Bodenmiller, B. cytomapper: an R / Bioconductor package for visualization of highly multiplexed imaging data. *Bioinformatics* **36**, 5706–5708 (2020).
- 1290

Figures

Fig. 1

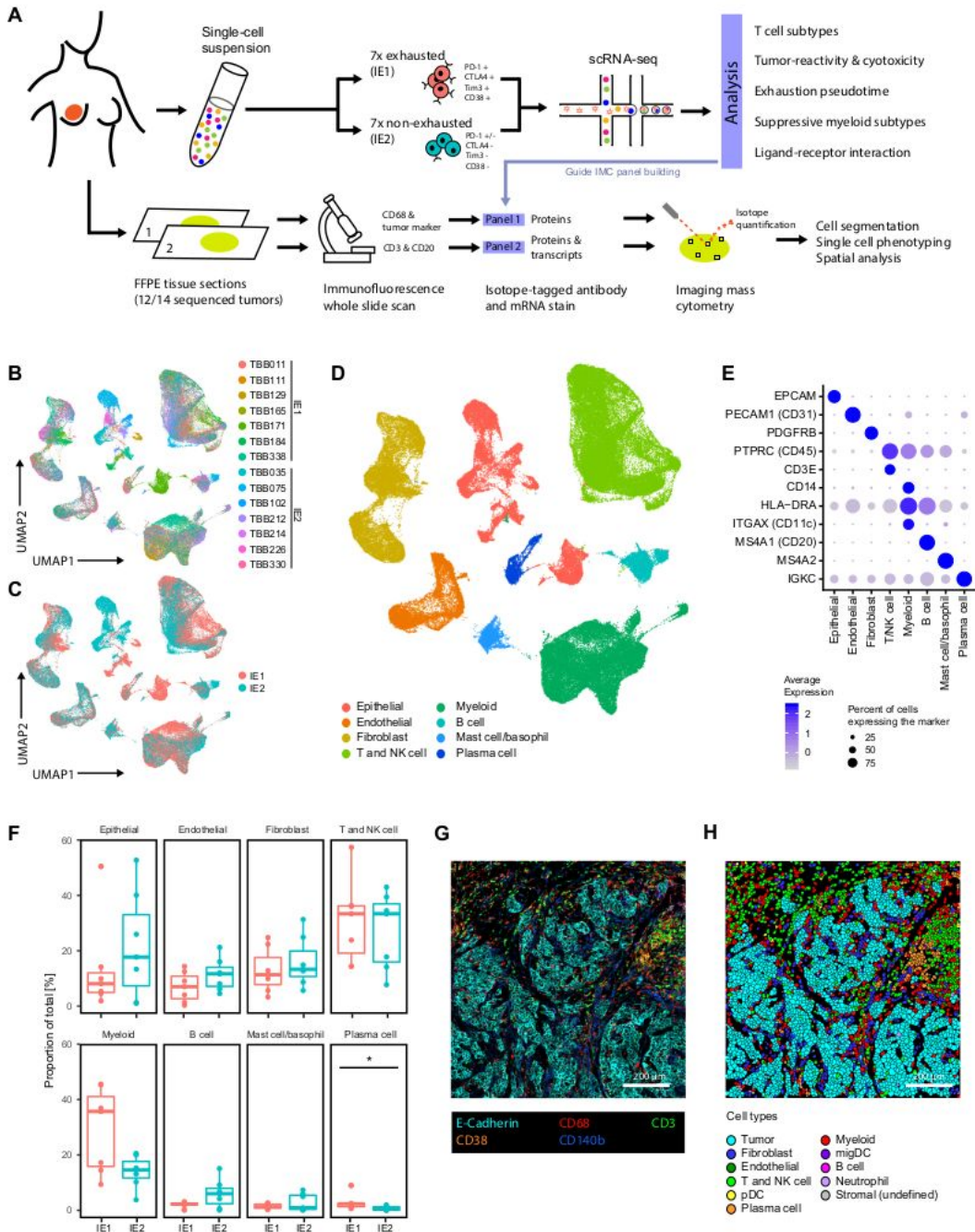


Figure 1

Transcriptomic and spatial proteomic analysis of breast tumor immune environments A. Sample selection and experimental approach. B. UMAP plot of scRNA-seq data from all 120,000 cells colored by patient. C. UMAP plot of scRNA-seq data colored by immune environment (IE). D. UMAP plot of scRNA-

seq data colored by cell type. E. DotPlot showing transcript expression of main cell type markers in the indicated cell subsets. F. Proportion (% of total cells) of main cell types in IE1 and IE2 tumors. Wilcoxon rank sum test was used for statistical analysis. * $p < 0.05$. Boxplot bodies show interquartile ranges (IQR), and whiskers extend to the largest and the smallest value within 1.5 times the IQR above the 75th percentile and below the 25th percentile, respectively. G. Exemplary IMC image showing staining patterns for the indicated markers. H. Single-cell masks for the IMC image displayed in panel G colored by cell type.

Fig. 2

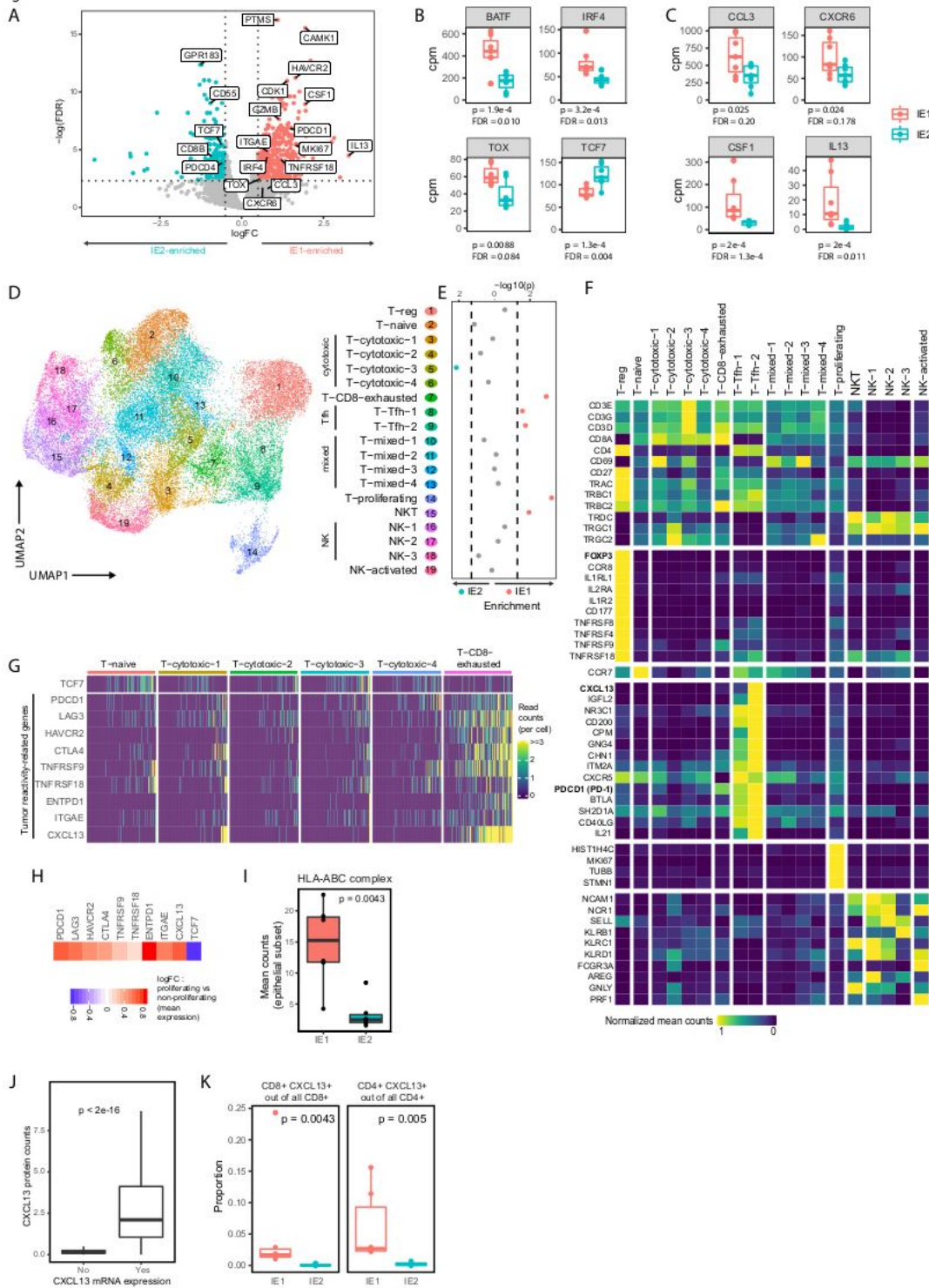


Figure 2

The T cell phenotypic landscape of exhausted and non-exhausted immune environments A. Volcano plot showing differential gene expression between T and NK cells of IE1 and IE2 samples in pseudobulk patient-averaged scRNA-seq data. Dashed lines indicate a false discovery rate (FDR) of 0.1 and a log₂ fold change (log₂FC) of 0.5. B. Boxplots comparing the T and NK pseudobulk expression in counts per million (cpm) of selected transcription factors in IE1 and IE2 samples. C. Boxplots comparing the T and NK pseudobulk expression in cpm of selected cytokines and receptors in IE1 and IE2 samples. D. UMAP plot of scRNA-seq data from 36,000 T and NK cell cells colored by Seurat cluster, annotated with the indicated cell type labels. E. Enrichment of cluster frequencies, annotated by cell type, in IE1 or IE2 samples. Wilcoxon rank sum test was used for statistical analysis and dashed lines indicate a p value of 0.05. F. Heatmap showing normalized average expression of selected marker genes for all T and NK cell clusters. G. Single-cell count heatmap of selected genes associated with tumor-reactivity and/or exhaustion. For this analysis, 100 cells were randomly sampled from the naïve T cell cluster and from each CD8⁺ T cell cluster; columns represent single cells. H. Heatmap displaying the log-fold change of the mean expression of the indicated genes in proliferating versus non-proliferating T and NK cells. I. Boxplot comparing the mean single-cell HLA-ABC expression in IMC data for the epithelial subsets of IE1 versus IE2 samples. J. Boxplot comparing mean CXCL13 protein counts between CXCL13-expressing and non-expressing T cells in IMC data. K. Boxplot comparing CXCL13^{high} cell proportions out of all CD8⁺ T cells (left) and CD4⁺ T cells (right) between IMC IE1 and IE2 samples. Only non-TLS images were included and Wilcoxon rank sum test was used for statistical analysis. For scatterplots, Spearman correlation coefficient and p value are indicated. For boxplots, Wilcoxon rank sum test was used for statistical analysis. Boxplot bodies show IQR, and whiskers extend to the largest and the smallest value lying within 1.5 times the IQR above the 75th percentile and below the 25th percentile, respectively.

Figure 3

Cytotoxic effector profiles differ between exhausted and non-exhausted immune environments A. Bar plot showing differential expression of the indicated transcripts in T and NK cells between IE1 and IE2 tumors (patient-averaged pseudobulk data). B. Heatmap showing normalized average single-cell expression of cytotoxic genes for all T and NK cell clusters. C. Pseudotime ordering of CD8⁺ T cells in all samples based on scRNA-seq data. Single cells are colored according to metacluster (bottom) and the corresponding density plot is displayed (top). D. Mean pseudotime scores for individual cell phenotype clusters. E. Mean pseudotime scores for individual samples colored by immune environment. F. Single-cell expression of the indicated cytotoxic genes along pseudotime. The analysis was done on scRNA-seq data from CD8⁺ T cells in all samples. Red line corresponds to locally estimated scatterplot smoothing (LOESS) curve. G. Average single-cell CSF1 expression in all T and NK cell clusters displayed as a bar chart (top) and in a normalized heatmap (bottom).

Figure 4

Myeloid cell phenotypes in exhausted immune environments indicate inflammation and T cell-suppressive potential. A. Volcano plot showing differential gene expression between myeloid cells of IE1 and IE2 samples in pseudobulk patient-averaged scRNA-seq data. Dashed lines indicate an FDR of 0.1 and a logFC of 0.5. Genes are colored by functional group. B. UMAP plot of scRNA-seq data from 26,000 myeloid cells colored by Seurat cluster and annotated by cell type. C. Enrichment of cluster frequencies in IE1 and IE2 samples. Wilcoxon rank sum test was used for statistical analysis and dashed lines indicate a p value of 0.05. D. Heatmap showing normalized average single-cell expression of the top 10 differentially expressed genes for all myeloid cell clusters. Selected genes overexpressed in the respective cluster are indicated in the colored boxes. E. Scatterplot of the mean T cell-suppression score versus the mean T cell attraction score for all myeloid cell clusters. F. DotPlot showing expression of main migDC markers across all myeloid cell clusters. G. UMAP of cDC subsets and migDCs with Slingshot trajectories overlaid. H. Slingshot pseudotime ordering of single cells from the cDC2 and migDC subsets (top) and heatmap showing normalized expression of selected genes along pseudotime using the rolling average expression over 11 cells (bottom). Genes with log counts per million < 1.5 in EdgeR analysis were excluded for plots A-D. For scatterplots, Spearman correlation coefficient and p value are indicated.

Fig. 5

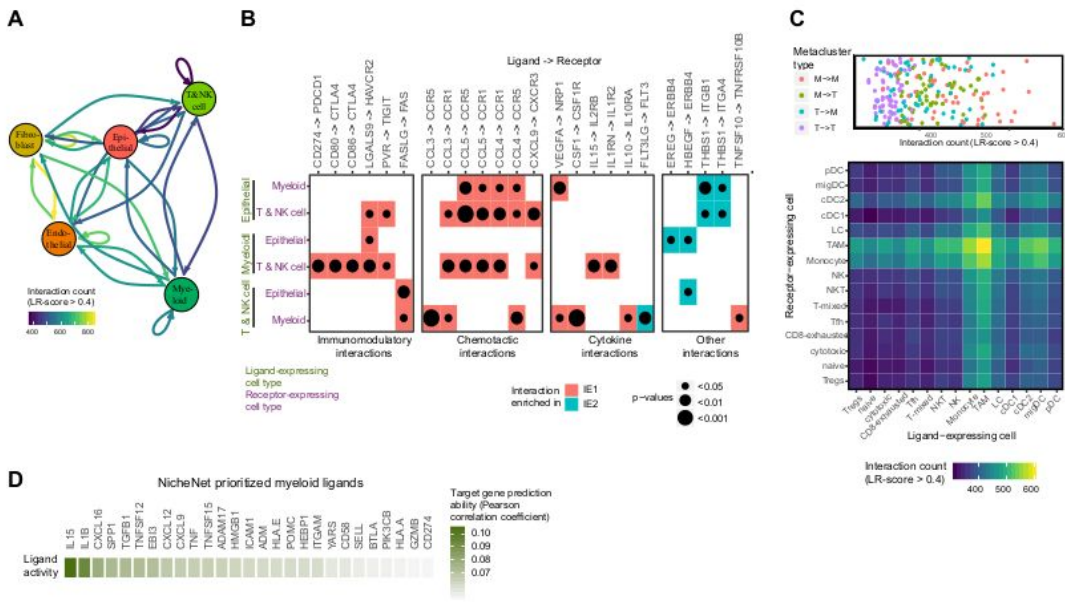


Figure 5

Ligand-receptor analysis predicts TIME-wide and exhaustion-specific cellular crosstalk A. Social graph depicting the number of interactions between the five most frequent cell types. B. Enrichment of selected ligand-receptor interactions in either IE1 or IE2 tumors for the given cell type pairs. Selections were made based on literature evidence and biological interpretability. The full list of enriched interaction pairs is in Supplementary Table 6. White squares denote interactions with an enrichment p value > 0.05 or a mean

LR score < 0.4 in the given cell type pair. Wilcoxon rank sum test was used for statistical analysis. C. DotPlot (top) and heatmap (bottom) depicting the number of interactions between different myeloid and T and NK cell metaclusters. M indicates myeloid metacluster; T indicates T and NK cell metacluster. D. Heatmap showing the myeloid-derived ligands with the highest ability to affect exhaustion-related target gene expression as predicted by NicheNet.

Figure 6

IMC reveals cellular neighborhoods, cytokine milieus and tertiary lymphoid structures A. Heat map indicating significant pairwise cell type interaction or avoidance summarized across the two-sided permutation tests on the individual images of the Protein Panel dataset (n = 77 images, 1,000 permutations each). Square color indicates the percentage of images with a significant cell-cell interaction or avoidance ($P < 0.01$), corrected for relative cell type frequency. Highlighted interactions (numbered boxes) indicate (1) fibroblast-endothelial interactions (2) myeloid autointeractions, (3) tumor compartment, (4) hypoxic/apoptotic tumor cell to immune cell interactions, (5) tumor to T cell subtype interactions, (6) main immune compartment, and (7) migDC-PD-1^{high} T cell interaction. B. Single-cell masks for selected IMC images (top: mature TLS image, bottom: immature TLS image) colored by cell subtype. Only a subsection of each image is shown. C. Paired box plot comparing the percentage of PD-1^{high} T cells versus PD-1^{low} T cells that have at least one migDC as a direct neighbor. Each pair of dots represents a separate sample. A paired Wilcoxon rank sum test was used for statistical analysis. D. Heatmap displaying the average relative proportion of each celltype among the 10 nearest neighbours for each T cell subtype across all non-TLS images. E. Heatmap indicating significant relative enrichment or depletion of each cell type in the different cytokine milieus summarized across the Fisher's exact tests on all individual images of the RNA Panel dataset (total = 77 images; for each individual combination, only images containing the respective community and the respective cell type were included). F. Single-cell masks for selected IMC images with cell outline colored by the indicated cytokine community and cell body colored by cell type. G. Stacked barplots indicating the slide-wide TLS status for a cohort of 13 IE1 samples and 12 IE2 samples. H. Stacked barplots showing the proportions of CXCL13⁺ T cells that are part of a CXCL13-cytokine-cluster for non-TLS, immature TLS, and mature TLS images.

Supplementary Files

This is a list of supplementary files associated with this preprint. Click to download.

- [Tables.zip](#)
- [TietscherSupplementalFiguresplusLegends.pdf](#)